Chapter 4

Natural Element Method for Two-Dimensional Elasticity

In this Chapter, we discuss the application of the natural element method to boundary value problems in two-dimensional linear elasticity. To this end, we first present the treatment of material discontinuities using NEM, and then describe the methodology to model non-convex bodies, such as two-dimensional bodies with cracks. Using the variational framework and Galerkin procedure outlined in Chapter 2, the weak form for two-dimensional linear elasticity and the discrete system of equations for the natural element method are developed. Finally, numerical results for various boundary value problems in two-dimensional elastostatics are presented.

4.1 Treatment of Material Discontinuities

The treatment of material discontinuities in a two-dimensional setting using NEM is presented. Some typical examples of material discontinuities are encountered in composite materials, phase-transformations, and inclusions in a matrix with different material properties. A nice exposition on the underlying variational formulation and

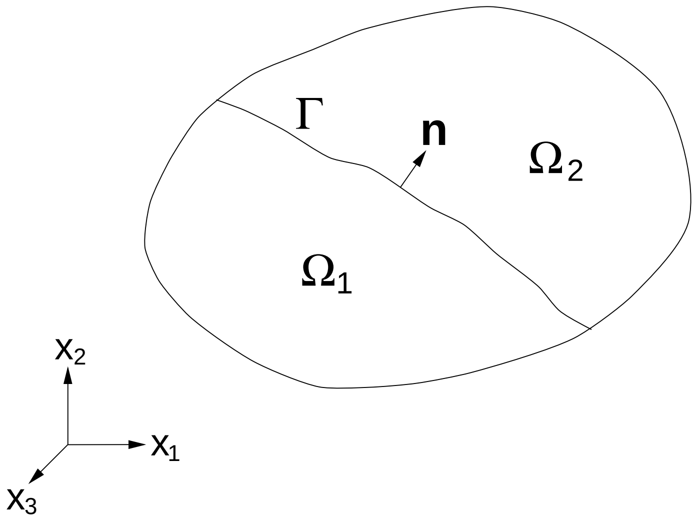

Figure 4.1: Bimaterial configuration ($\Omega = \Omega_1 \cup \Omega_2$).

finite element computations for this problem can be found in Mackinnon and Carey (1987).

Consider a two-dimensional body Ω, such that $\Omega = \Omega_1 \cup \Omega_2$, where Ω_1 and Ω_2 have different material properties. The interface between the two regions is Γ (Fig. 4.1). Since kinematically admissible displacement fields must be C^0, it is evident that displacement continuity must be met along the interface: $\mathbf{u}^1 = \mathbf{u}^2$ on Γ. An additional condition arises out of the variational principle—apart from the Euler-Lagrange equations, the natural interface condition is to be satisfied (in a weak sense), namely $\mathbf{t}^1 = \mathbf{t}^2$ along Γ. The above two conditions are automatically satisfied by the finite element interpolant if element boundaries are coincident with the discontinuity interface Γ. This is so, since the displacements are C^0, which allows for displacement gradients to be discontinuous in the normal direction ($\mathbf{n}$) to Γ.

The modeling of material discontinuities in the context of NEM follows. If the interface Γ is straight, then the description on convex domains in Section 3.3.9 holds, and the displacement field $\mathbf{u}$ along Γ is strictly linear between adjacent nodes. Therefore, for this case, the interface displacement and traction continuity conditions are met. Of course, here, unlike FEM, one must explicitly disallow points in Ω_1 to be influenced by nodes in Ω_2 and vice-versa. A line-of-sight or visibility criterion (Belytschko et al., 1996), similar to that used by Cordes and Moran (1996) is invoked to meet the above requirement. Now, let us consider the case where either Ω_1 or Ω_2 is a non-convex domain. A plate consisting of a quarter-circle is considered. The circular domain Ω_1 is convex, while Ω_2 is non-convex. The circular arc is the material interface Γ that demarcates the two regions. The displacements along Γ are linear when approaching the interface from Ω_1, but are not so when approaching from Ω_2. In Section 3.3.9, the linearity of the displacement field along Γ for the domain Ω_2 is discussed. As indicated in Section 3.3.9, with sufficient nodal discretization of the interface Γ, the linearity of the displacement field can be met to within a desired tolerance ϵ. Since the trial functions are no longer C^0, the numerical implementation assumes the form of a non-conforming method. In Section 4.4.6, the problem of an inclusion in an infinite matrix is solved using NEM. For the grid shown in Fig. 4.19 with 13 nodes along Γ, the displacement discontinuity across Γ is less than 1% of the displacement values on either side.

4.2 Modeling of Non-Convex Bodies

The modeling of non-convex bodies, such as two-dimensional straight or curved cracks using the natural element method is addressed. Cracks are straight or curved lines of discontinuity in a two-dimensional body. From a modeling perspective, the numerical formulation must permit a displacement discontinuity to exist across the crack line. In finite elements, this is facilitated by having coincident nodes with independent degrees of freedom along the line of discontinuity.

Consider a non-convex domain with a straight edge-crack, which is modeled using two distinct crack faces LC and MC (Fig. 4.2). The finite separation between the crack faces is illustrated for ease of exposition. Akin to the finite element method, one can also use coincident nodes with independent degrees of freedom along the crack line. In Fig. 4.2a, the nodes and the crack surfaces are shown while in Fig. 4.2b, the Delaunay triangles and the natural neighbor circumcircles for two triangles are presented. The triangulation of non-convex planar domains can be carried out using either conforming or constrained triangulation (Lo, 1989; Borgers, 1990). In a conforming triangulation, the empty circumcircle property is preserved, and the triangulation is the strict dual of the Voronoi diagram, while in a constrained triangulation, the duality property does not hold. In Fig. 4.2b, the triangulation shown is a conforming one, which ensures the duality with the Voronoi diagram. In order to include the crack surfaces in the numerical modeling, the crack faces LC and MC are treated as boundaries for the upper and lower regions, respectively. In effect, for the domain above the crack line, the Voronoi cells for the nodes along LC are unbounded, while for the domain below the crack line, the Voronoi cells for the nodes along the boundary MC are unbounded. If we construct the circumcircles for $\triangle_{ABC}$ and $\triangle_{CDE}$ as shown in Fig. 4.2b, the above description of crack modeling implies that nodes C, D, and E are natural neighbors of point $\mathbf{x}$, while nodes A and B are not. The above approach preserves the continuity of the trial function, and hence does not introduce any non-conformities in its implementation. In the modeling of crack problems where symmetry (two-fold or four-fold) can be invoked such that the domain of interest is convex, no modifications in NEM are required.

4.2.1 Enriching the Interpolant for Crack Problems

The shape functions $\phi_I(\mathbf{x})$ form a partition of unity. As indicated in Section 3.3.2, this facilitates the enrichment of the NEM trial function for crack problems, along similar lines as suggested by Melenk and Babuška (1996). In finite elements, the quarter-point element results in $\sqrt{r}$ behavior in the displacement field along rays emanating from the crack-tip. Since the exact displacement field solution for crack problems is $\mathcal{O}(\sqrt{r})$, this enhancement permits accurate modeling of the radial dependence of the crack-tip field in two-dimensions. In the context of NEM, one can extrinsically enhance the trial function by adding terms that have local $\sqrt{r}$ behavior. Let $\Omega_0 \subset \Omega$ be a sub-domain in a region around the crack-tip where the crack-tip singularity dominates. Then the enriched trial function for two-dimensional crack problems assumes the form:

$$u_i^h(\mathbf{x}) = \sum_{I=1}^{n} \phi_I(\mathbf{x}) u_{Ii} + \sqrt{r} \sum_{\substack{J=1 \\ \mathbf{x}_J \in \Omega_0}}^{m} \phi_J(\mathbf{x}) a_{Ji} \quad (i = 1,\, 2), \tag{4.1}$$

where a_{Ji} are additional nodal coefficients that are associated with the m nodes in Ω_0. The above form indicates that by incorporating the enrichment over the support of the nodes in Ω_0, the crack-tip displacement field is accurately modeled. Enriching FEM along similar lines could provide enriched trial function spaces of wider-scope and possibly better merit than the quarter-point element. In this thesis, the enriched interpolant is not used for the crack problem presented in Section 4.4.7; the NEM trial function given in Eq. (3.6) is used.

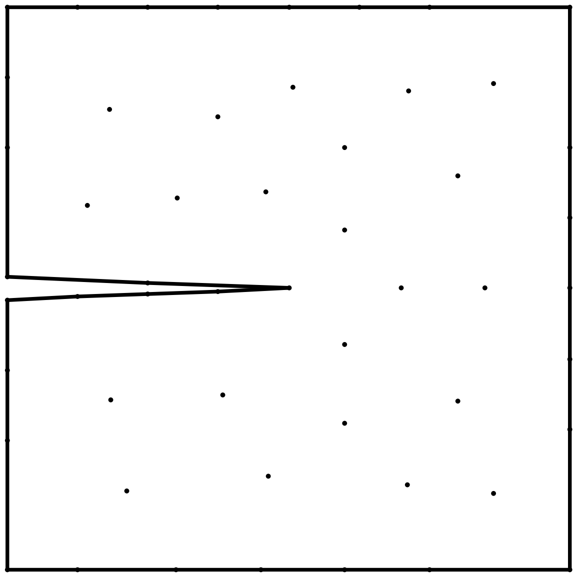

(a)

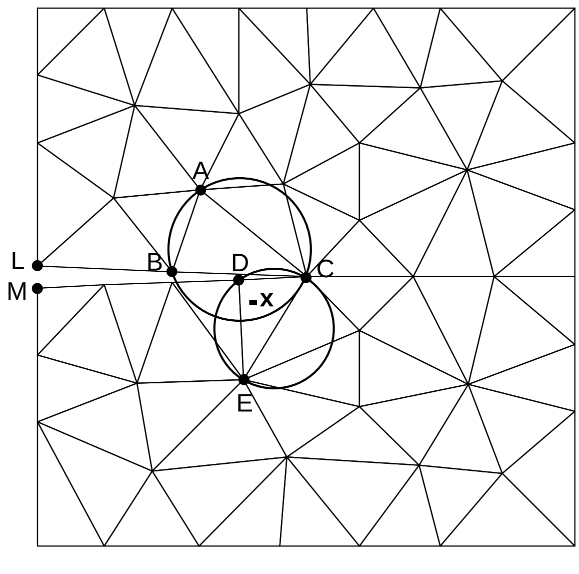

(b)

Figure 4.2: Crack modeling. (a) Nodes, and (b) Conforming triangulation.

4.3 Governing Equations and Weak Form

4.3.1 Strong Form

Consider a body which is described by an open bounded domain $\Omega \subset \mathbb{R}^2$, with boundary Γ. The set Γ is partitioned into two sets Γ_u (essential boundary) and Γ_t (natural boundary), with $\Gamma = \Gamma_u \cup \Gamma_t$ and $\Gamma_u \cup \Gamma_t = \emptyset$. The boundary value problem of elastostatics models the displacement $\mathbf{u}(\mathbf{x})$ of a body Ω which is fixed along Γ_u and subjected to surface forces (tractions) along Γ_t (Fig. 4.3). We now consider the

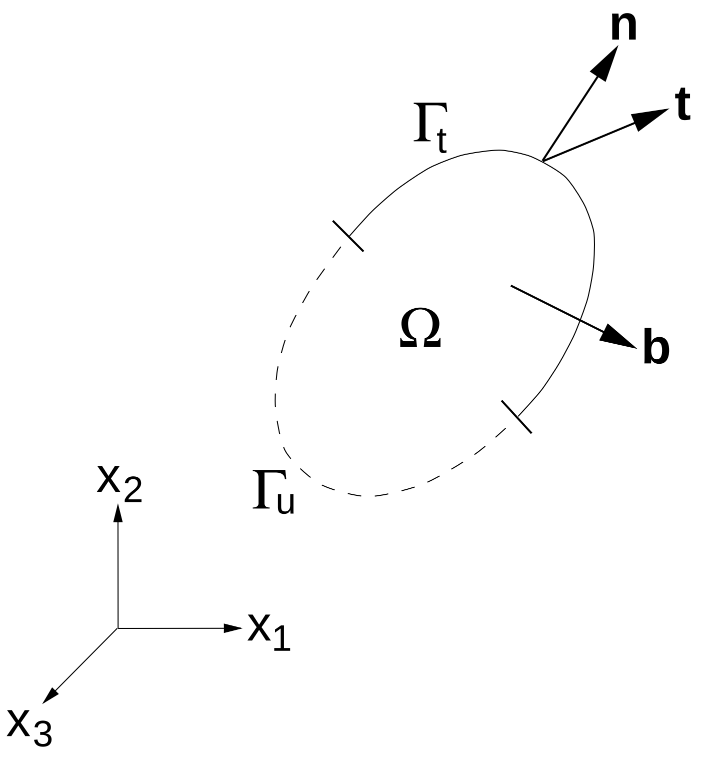

Figure 4.3: Elastostatic boundary value problem.

boundary value problem for small displacement elastostatics. The field equations of elastostatics are:

$$\sigma_{ji,j} + b_i = 0 \quad \text{in} \quad \Omega, \tag{4.2a}$$

$$\sigma_{ij} = \sigma_{ji}, \tag{4.2b}$$

$$\sigma_{ij} = C_{ijkl}(\varepsilon_{kl} - \varepsilon^*_{kl}), \tag{4.2c}$$

$$\varepsilon_{ij} = \frac{1}{2}(u_{i,j} + u_{j,i}), \tag{4.2d}$$

where $\mathbf{C}$ is the material moduli tensor which for a homogeneous isotropic material with material parameters λ and μ (Lamé constants) is given by

$$C_{ijkl} = \lambda\delta_{ij}\delta_{kl} + \mu(\delta_{ik}\delta_{jl} + \delta_{il}\delta_{jk}). \tag{4.2e}$$

The Einstein summation convention on repeated indices is implied in Eq. (4.2), and the indices i, j, k, and l take on values 1, 2, and 3. In Eq. (4.2), σ_{ij} is the Cauchy stress for a kinematically admissible displacement field u_i, ε_{ij} is the small strain tensor, b_i is the body force per unit volume, and ε^*_{kl} is an imposed eigenstrain tensor. Equation (4.2a) is the equilibrium equation of elastostatics (conservation of linear momentum); the symmetry of the Cauchy stress in Eq. (4.2b) is a consequence of the conservation of angular momentum; Eq. (4.2c) is the linear elastic constitutive relation; and Eq. (4.2d) is the kinematic relation between the small strain tensor and the displacement vector. The eigenstrain tensor given in Eq. (4.2c) is included in the formulation to permit the treatment of a transformation strain problem that appears in Section 4.4.6.

Displacement (essential) boundary conditions are imposed on Γ_u and traction (natural) boundary condition on Γ_t. The essential and natural boundary conditions are:

$$u_i = \bar{u}_i \quad \text{on} \quad \Gamma_u, \tag{4.3a}$$

$$t_i = \sigma_{ji} n_j = \bar{t}_i \quad \text{on} \quad \Gamma_t, \tag{4.3b}$$

where n_i is the unit outward normal to Ω, and $\bar{u}_i$ and $\bar{t}_i$ are prescribed displacements and tractions, respectively.

4.3.2 Weak Form

Let $\mathbf{u}$ be the displacement solution for an elastostatic boundary value problem, with $\boldsymbol{\sigma}(\mathbf{u})$ the corresponding Cauchy stress tensor. In the absence of inertial forces, the Cauchy stress σ_{ij} satisfies the equilibrium equation of elastostatics:

$$\sigma_{ji,j} + b_i = 0 \quad \text{in} \quad \Omega. \tag{4.4}$$

The equilibrium equation is a set of two coupled second-order ($m = 1$) elliptic partial differential equations. On the basis of the exposition in Section 2.2, we choose the displacement trial solution $\mathbf{u} \in \mathbf{V} = \left(H^1(\Omega)\right)^2$, and let $\mathbf{v} \in \mathbf{V}_0 = \left(H_0^1(\Omega)\right)^2$ be any set of kinematically admissible test functions (virtual displacements). The Sobolev spaces $H^1(\Omega)$ and $H_0^1(\Omega)$ are defined in Section 2.1.1. On multiplying Eq. (4.4) by v_i and integrating over Ω, we obtain

$$\int_\Omega \sigma_{ji,j} v_i \, d\Omega + \int_\Omega b_i v_i \, d\Omega = 0. \tag{4.5}$$

Re-writing the first integral in terms of the gradient of the product $\sigma_{ji}v_i$, we have

$$\int_\Omega (\sigma_{ji}v_i)_{,j}\, d\Omega - \int_\Omega \sigma_{ji}v_{i,j}\, d\Omega + \int_\Omega b_i v_i\, d\Omega = 0. \tag{4.6}$$

On using Green's formula from Eq. (2.19a) in Eq. (4.6), we obtain

$$\int_\Gamma \sigma_{ji}n_j v_i\, d\Gamma - \int_\Omega \sigma_{ji}v_{i,j}\, d\Omega + \int_\Omega b_i v_i\, d\Omega = 0. \tag{4.7}$$

By invoking Cauchy's formula given in Eq. (4.3b), the above equation takes the form

$$\int_\Gamma \bar{t}_i v_i\, d\Gamma - \int_\Omega \sigma_{ji}v_{i,j}\, d\Omega + \int_\Omega b_i v_i\, d\Omega = 0. \tag{4.8}$$

Since $\boldsymbol{\sigma}$ is a symmetric second-order tensor ($\sigma_{ij} = \sigma_{ji}$), we have the relation:

$$\sigma_{ji}v_{i,j} = \frac{\sigma_{ij}}{2}(v_{i,j} + v_{j,i}) = \sigma_{ij}(\mathbf{u})\varepsilon_{ij}(\mathbf{v}), \tag{4.9}$$

where the explicit dependence on the trial and test functions is indicated. On substituting the above identity in Eq. (4.8) and re-arranging the terms, we obtain

$$\int_\Omega \sigma_{ij}(\mathbf{u})\varepsilon_{ij}(\mathbf{v})\, d\Omega = \int_\Omega b_i v_i\, d\Omega + \int_\Gamma \bar{t}_i v_i\, d\Gamma. \tag{4.10}$$

Since the test functions v_i vanish on the essential boundary Γ_u, we obtain the result:

$$\boxed{\begin{array}{c}\text{Find } \mathbf{u} \in \mathbf{V} \text{ such that} \\ \displaystyle\int_\Omega \boldsymbol{\sigma}(\mathbf{u}) : \boldsymbol{\varepsilon}(\mathbf{v})\, d\Omega = \int_\Omega \mathbf{b}\cdot\mathbf{v}\, d\Omega + \int_{\Gamma_t} \bar{\mathbf{t}}\cdot\mathbf{v}\, d\Gamma \quad \forall\, \mathbf{v} \in \mathbf{V}_0.\end{array}} \tag{4.11}$$

Equation (4.11) is the weak or variational form of the equilibrium equation of linear elastostatics. In solid mechanics, the weak form is also referred to as the principle of virtual work. By using the constitutive relation given in Eqs. (4.2c) and (4.2e), we can write Eq. (4.11) in the variational framework indicated in Eq. (2.15) (see Chapter 2):

$$\begin{aligned} &\text{Find } \mathbf{u} \in \mathbf{V} \text{ such that} \\ &a(\mathbf{u}, \mathbf{v}) = \langle l, \mathbf{v} \rangle \quad \forall\, \mathbf{v} \in \mathbf{V}_0, \end{aligned} \tag{4.12a}$$

where

$$a(\mathbf{u}, \mathbf{v}) = 2\mu\big(\boldsymbol{\varepsilon}(\mathbf{u}), \boldsymbol{\varepsilon}(\mathbf{v})\big) + \lambda(\operatorname{div}\, \mathbf{u}, \operatorname{div}\, \mathbf{v}), \tag{4.12b}$$

$$\langle l, \mathbf{v} \rangle = (\mathbf{b}, \mathbf{v}) + (\bar{\mathbf{t}}, \mathbf{v}). \tag{4.12c}$$

In the above equations, the $L^2(\Omega)$ inner product for vectors and second-order tensors is defined as:

$$(\mathbf{u}, \mathbf{v}) = \int_\Omega \mathbf{u} \cdot \mathbf{v}\, d\Omega, \quad (\mathbf{A}, \mathbf{B}) = \int_\Omega \mathbf{A} : \mathbf{B}\, d\Omega, \tag{4.13}$$

where $\mathbf{u}$ and $\mathbf{v}$ are vectors, and $\mathbf{A} : \mathbf{B} = A_{ij} B_{ij}$ is the scalar product (double contraction) for symmetric second-order tensors $\mathbf{A}$ and $\mathbf{B}$ (Malvern, 1969).

4.3.3 Discrete System and NEM Implementation

Consider the Bubnov-Galerkin implementation for the natural element method in two-dimensional linear elasticity. In the natural element method, finite-dimensional subspaces $\mathbf{V}^h \subset \mathbf{V}$ and $\mathbf{V}_0^h \subset \mathbf{V}_0$ are used as the approximating trial and test spaces. The weak form for the discrete problem can be stated as:

$$\text{Find } \mathbf{u}^h \in \mathbf{V}^h \subset \mathbf{V} \quad \text{such that}$$
$$\int_{\Omega^h} \boldsymbol{\sigma}(\mathbf{u}^h) : \boldsymbol{\varepsilon}(\mathbf{v}^h) = \int_{\Omega^h} \mathbf{b} \cdot \mathbf{v} \, d\Omega + \int_{\Gamma^h} \bar{\mathbf{t}} \cdot \mathbf{v} \, d\Gamma \quad \forall \, \mathbf{v}^h \in \mathbf{V}_0^h \subset \mathbf{V}_0. \tag{4.14}$$

In a Bubnov-Galerkin procedure, the trial functions $\mathbf{u}^h$ as well as the test functions $\mathbf{v}^h$ are represented as linear combinations of the same shape functions. The trial and test functions are

$$\mathbf{u}^h(\mathbf{x}) = \sum_{I=1}^{n} \phi_I(\mathbf{x}) \mathbf{u}_I, \quad \mathbf{v}^h(\mathbf{x}) = \sum_{I=1}^{n} \phi_I(\mathbf{x}) \mathbf{v}_I. \tag{4.15}$$

On substituting the trial and test functions from Eq. (4.15) in Eq. (4.14), and using the arbitrariness of nodal variations, the following discrete system of linear equations is obtained:

$$\boldsymbol{K}\mathbf{d} = \mathbf{f}, \tag{4.16}$$

where

$$\mathbf{K}_{IJ} = \int_{\Omega^h} \mathbf{B}_I^T \mathbf{C} \mathbf{B}_J \, d\Omega, \tag{4.17a}$$
$$\mathbf{f}_I = \int_{\Gamma_t^h} \phi_I \bar{\mathbf{t}} \, d\Gamma + \int_{\Omega^h} \phi_I \mathbf{b} \, d\Omega + \int_{\Omega^h} \boldsymbol{B}_I^T \mathbf{C} \boldsymbol{\varepsilon}^* \, d\Omega. \tag{4.17b}$$

In the above equations, $\mathbf{B}_I$ is the matrix of shape function derivatives which is given by

$$\boldsymbol{B}_I = \begin{bmatrix} \phi_{I,x} & 0 \\ 0 & \phi_{I,y} \\ \phi_{I,y} & \phi_{I,x} \end{bmatrix}. \tag{4.18}$$

The constitutive matrix $\boldsymbol{C}$ for an isotropic linear elastic material is:

$$\boldsymbol{C} = \frac{E}{(1-2\nu)(1+\nu)} \begin{bmatrix} 1-\nu & \nu & 0 \\ \nu & 1-\nu & 0 \\ 0 & 0 & \dfrac{1-2\nu}{2} \end{bmatrix} \qquad \text{(plane strain)}, \tag{4.19a}$$

$$\boldsymbol{C} = \frac{E}{(1-\nu^2)} \begin{bmatrix} 1 & \nu & 0 \\ \nu & 1 & 0 \\ 0 & 0 & \dfrac{1-\nu}{2} \end{bmatrix} \qquad \text{(plane stress)}. \tag{4.19b}$$

In the context of the natural element method, the stiffness matrix $\mathbf{K}$ and external force vector $\mathbf{f}$ given in Eq. (4.17) are assembled on a nodal basis. This choice is necessitated due to the absence of an inherent element structure in NEM, as opposed to the finite element method where shape functions are constructed on the basis of elements. In addition, the stiffness matrix in NEM is symmetric and sparse, but not necessarily banded. The Delaunay triangles are used as the background integration cells for the numerical integration computations. It is to be noted that the Delaunay triangulation is just one among many choices to partition the domain for the purpose of numerical integration of the weak form; quadrilaterals or octree-based cell structures are also suitable choices for the numerical integration computations. An alternative approach proposed by Traversoni (1994) involves carrying out the numerical integration over the area of intersection of circumcircles. The idea is appealing since tensor product terms such as $\phi_{I,i}\phi_{J,j}$ are non-zero over the area of intersection of circumcircles about nodes n_I and n_J. In spite of its merits, the mappings and transformations involved appear to be non-trivial, with no cubature scheme currently known for such domains. Hence this approach is not pursued in this work, and the Delaunay triangles themselves are used in the numerical integration of the weak form.

4.4 Numerical Results and Discussions

The application of NEM to problems in small displacement two-dimensional elastostatics, in the absence of body forces, is presented. Unless stated otherwise, the material properties chosen in the analyses are: $E = 3 \times 10^7$ psi and $\nu = 0.25$. Numerical integration is carried out using symmetric quadrature rules for a triangle (Lyness and Jespersen, 1975; Dunavant, 1985). Three point quadrature rule is used in the numerical integration of the weak form; the error norm computations are carried out using 25 point quadrature rule in each triangle.

4.4.1 Eigenanalysis

In order to study the properties of the approximation spaces of NEM, we consider the linear independence of the shape functions (Strang and Fix, 1973). To this end, we consider the following discrete eigenvalue problem:

$$\mathbf{M}\hat{\mathbf{d}} = \lambda^h \hat{\mathbf{d}}, \tag{4.20}$$

where $\hat{\mathbf{d}}$ and λ^h are the eigenvectors and eigenvalues of $\mathbf{M}$, and $\mathbf{M}$ is the mass matrix (Gram matrix in linear algebra) which is given by

$$\mathbf{M}_{IJ} = \int_\Omega \phi_I \phi_J \, d\Omega. \tag{4.21}$$

The condition number $\kappa(\mathbf{M})$ of the matrix $\mathbf{M}$ is defined as the ratio of the maximum eigenvalue $\lambda_{\max}(\mathbf{M})$ to that of the minimum eigenvalue $\lambda_{\max}(\mathbf{M})$. The condition number is used as a measure of the linear independence of the shape functions. If the shape functions were orthonormal, $\mathbf{M}_{IJ}$ would be the identity matrix and $\kappa = 1$. The EISPACK (Smith, Boyle, Garbow, Ikebe, Klema, and Moler, 1974) eigensolver package is used to solve the eigenvalue problem. In Table 4.1, the condition number is computed for the nodal grid shown in Fig. 4.4a and uniform refinements of the same grid; in addition, results are also computed for the nodal grid shown in Fig. 4.4c and for the irregular focused grid in Fig. 4.21b that is used for the edge crack problem in Section 4.4.7. The condition numbers obtained for NEM are of the same order as constant strain finite elements for both the uniform and non-uniform nodal discretization which indicates that the matrix is well-conditioned and the approximation spaces are linearly independent.

4.4.2 Patch Tests

The patch test (Bazeley, Cheung, Irons, and Zienkiewicz, 1965; Irons and Razzaque, 1972) is the ubiquitous test for the convergence of non-conforming finite element methods. Even though there remains significant disagreement as to whether it is a necessary condition for convergence, its merit and use as a benchmark for the eval-

Table 4.1: Linear independence of C^0 shape functions.

<table>
<tr><th rowspan="3">Grids</th><th rowspan="3">Nodes</th><th colspan="2">κ^h_{NEM}</th><th rowspan="3">κ^h_{FEM}</th></tr>
<tr><th colspan="2">Quadrature</th></tr>
<tr><th>3</th><th>25</th></tr>
<tr><td rowspan="3">Uniform</td><td>25</td><td>3.99</td><td>3.83</td><td>7.00</td></tr>
<tr><td>289</td><td>3.99</td><td>3.83</td><td>7.00</td></tr>
<tr><td>4225</td><td>3.99</td><td>3.83</td><td>7.00</td></tr>
<tr><td rowspan="2">Non-uniform</td><td>70</td><td>50.86</td><td>35.65</td><td>43.17</td></tr>
<tr><td>278</td><td>2148.97</td><td>2146.45</td><td>3422.31</td></tr>
</table>

uation and validation of non-conforming elements is unquestionable. For a historical perspective and review of the patch test, see Felippa, Haugen, and Militello (1995). In the context of meshless methods, the relevance of the patch test from the viewpoint of convergence is still an open issue, which needs to be addressed and understood in a better light.

Displacement In the displacement patch test, a linear displacement field is imposed on the boundary Γ_u ($\Gamma_u = \partial\Omega$) of a domain Ω. If the patch test is passed, the linear displacement field is approximated exactly, and the numerical solution at the interior nodes should be in exact (within machine precision) agreement with the linear solution. This validates, apart from the consistency condition, the accuracy of the numerical integration of the weak form in the Galerkin implementation. In Fig. 4.4, three different nodal discretizations for a unit square are shown. In Fig. 4.4a, a uniform grid with 25 nodes is considered; an irregular grid (8 nodes) is shown in Fig. 4.4c; and in Fig. 4.4e, a random set of 70 nodes is chosen. It is noted that for the uniform nodal grid shown in Fig. 4.4a, the Delaunay triangles are non-unique, even though the Voronoi diagram for the set of nodes is unique. A valid Delaunay triangulation for the regular nodal discretization is shown in Fig. 4.4b. For the displacement patch test, a linear displacement field $u_i = x_i$ is imposed on the boundary nodes of the unit square. We remark here that if all diagonals of the Delaunay triangles for the grid shown in Fig. 4.4a are aligned in the same direction, the $L^2(\Omega)$ and $H^1(\Omega)$ error norm results for three point quadrature in each triangle are 10^{-16} and 10^{-15}, respectively. This is a fortuitous result that is attributable to symmetry in the location of the quadrature points and cancellations in the numerical integration. This result does not merit presentation, since it is an anomaly. We do point it out here to emphasize the fact that a systematic study with large number of numerical tests should be carried out in order to draw a sound inference or (numerically) prove a claim for that matter.

The NEM displacement patch test results for the relative $L^2(\Omega)$ error norm and relative $H^1(\Omega)$ error norm are presented in Table 4.2. The $L^2(\Omega)$ and $H^1(\Omega)$ error

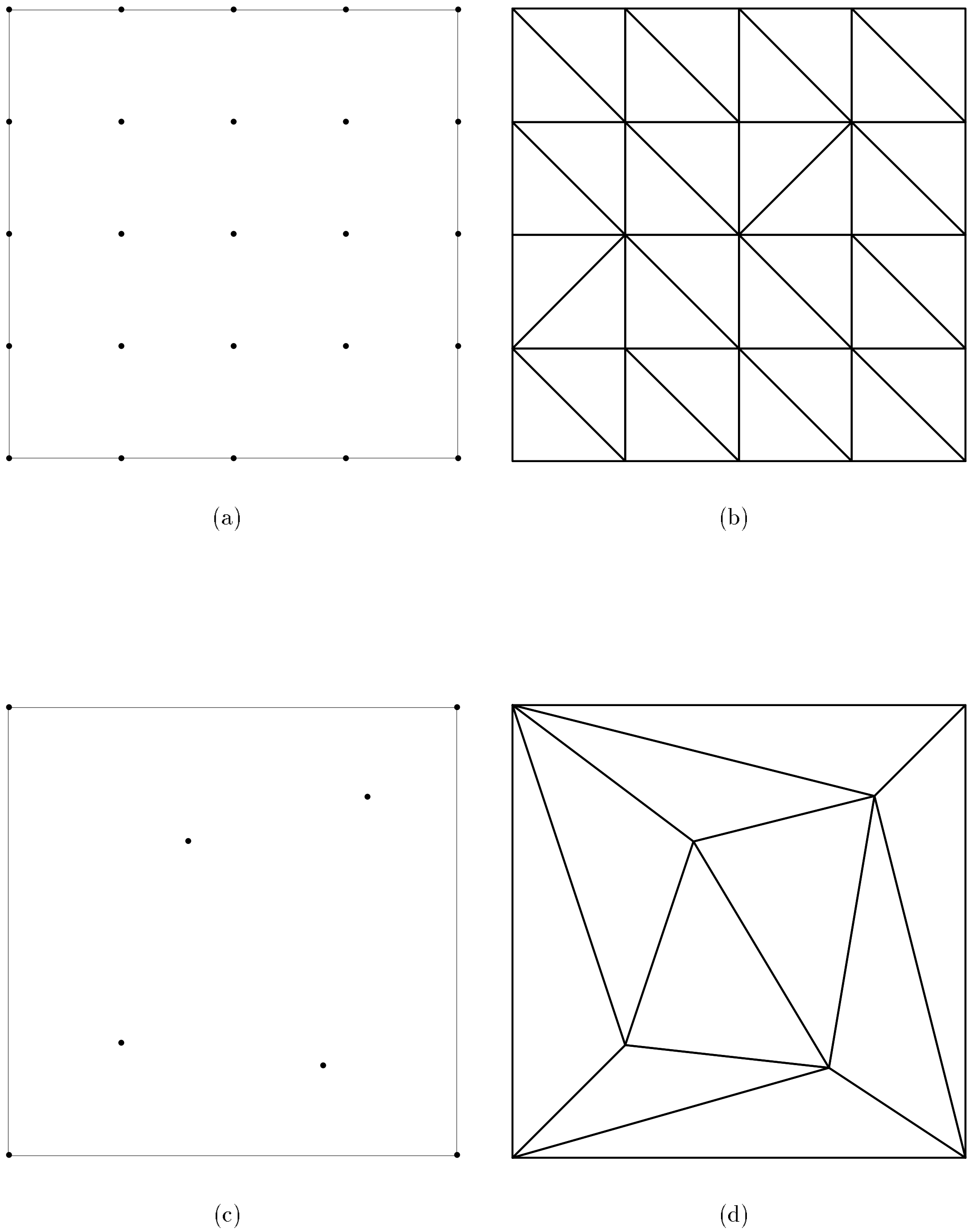

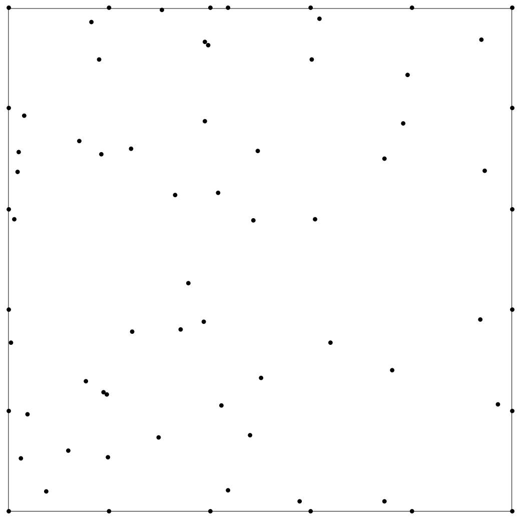

(e)

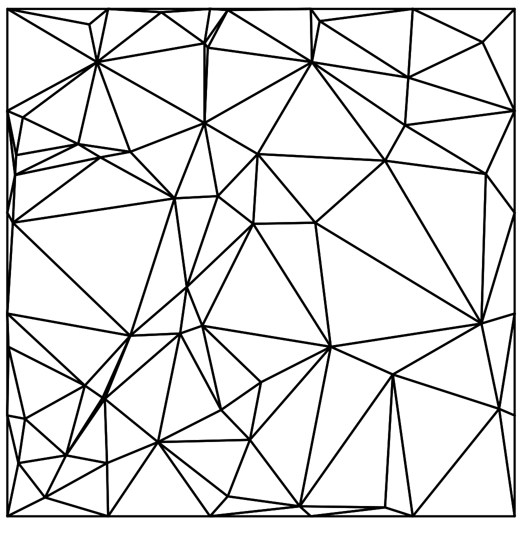

(f)

Figure 4.4: Displacement patch test. (a) and (b) Uniform grid (25 nodes), (c) and (d) Irregular grid (8 nodes), and (e) and (f) Random set (70 nodes).

norms are defined as follows:

$$\|\mathbf{u}-\mathbf{u}^h\|_{L^2(\Omega)} = \left(\int_\Omega (u_i - u_i^h)(u_i - u_i^h)\, d\Omega\right)^{1/2}, \tag{4.22a}$$

$$\|\mathbf{u}-\mathbf{u}^h\|_{H^1(\Omega)} = \left(\int_\Omega \left[(u_i - u_i^h)(u_i - u_i^h) + (u_{i,j} - u_{i,j}^h)(u_{i,j} - u_{i,j}^h)\right] d\Omega\right)^{1/2}, \tag{4.22b}$$

where $\mathbf{u}$ and $\mathbf{u}^h$ are the exact and numerical (NEM) displacement solutions, respectively. In Table 4.2, the results are shown for both, 3 point, as well 25 point quadrature within each Delaunay triangle. For the error norm computations, 25 point quadrature rule is used within each triangle. The error norm results indicate that the displacements and strains in the patch test are accurate to within 10^{-4} and 10^{-3}, respectively. Thus, since machine precision (double precision arithmetic) on a HP9000/s700 workstation is 10^{-16}, the patch test is not met with respect to this measure. Since the NEM interpolant can exactly reproduce a linear displacement field (Section 3.3.3), the numerical integration of the weak form is the source for the above discrepancy. Inexact numerical integration of the weak form (potential energy functional) is one of the variational crimes (Strang and Fix, 1973). In NEM, two factors lead to the numerical integration errors, namely, the non-polynomial form of the shape functions and the use of Delaunay triangles for numerical integration which are not coincident with the supports of the shape functions (Section 3.3.4). As indicated in Section 4.3.3, the natural domain for the numerical integration is the area of intersection (Ω_c) of natural neighbor circumcircles. There exist cubature rules with polynomial precision for two-dimensional domains such as, square, circle, triangle, and the plane (Stroud, 1971; Cools and Rabinowitz, 1997). In addition, adaptive numerical integration procedures for other planar domains that are affine transformation of the above primitives are also available (Cools, Laurie, and Pluym, 1997). However, no general polynomial precision scheme for the domain Ω_c is known. It is envisaged that an easy-to-implement and robust numerical cubature scheme over Ω_c that is specifically tailored to the NEM interpolant could lead to significant improvements in the numerical integration. The above shortcoming of NEM with respect to the patch test is also seen in meshless methods. For instance, in EFG, typical relative $L^2(\Omega)$ error norms in displacements are obtained to within 10^{-6} accuracy with high Gauss-Legendre product rules over quadrilaterals for numerical integration. This again, is due to inexact numerical integration of the weak form.

Table 4.2: Relative error norms for the displacement patch test.

Grids	Quadrature	$\dfrac{\Vert\mathbf{u}-\mathbf{u}^h\Vert_{L^2(\Omega)}}{\Vert\mathbf{u}\Vert_{L^2(\Omega)}}$	$\dfrac{\Vert\mathbf{u}-\mathbf{u}^h\Vert_{H^1(\Omega)}}{\Vert\mathbf{u}\Vert_{H^1(\Omega)}}$
a	3	7.5×10^{-4}	4.0×10^{-3}
	25	8.4×10^{-5}	4.5×10^{-4}
c	3	9.3×10^{-3}	4.1×10^{-2}
	25	1.1×10^{-3}	4.3×10^{-3}
e	3	4.4×10^{-3}	9.2×10^{-2}
	25	4.8×10^{-4}	7.9×10^{-3}

Equilibrium The ability to represent a uniaxial plane stress field is verified by the equilibrium patch test. Consider a unit square plate under a uniaxial stress $\sigma = 1$ psi (plane stress conditions) in the x_2-direction (Fig. 4.5). The essential boundary conditions are indicated in Fig. 4.5. The exact displacement solution is:

$$u_1 = \frac{\nu}{E}(1 - x_1), \tag{4.23a}$$

$$u_2 = \frac{x_2}{E}. \tag{4.23b}$$

The three different nodal grids shown in Fig. 4.4 are considered for the equilibrium patch test, and the relative error norm results are presented in Table 4.3. In Table 4.3, the energy norm $\|\mathbf{u} - \mathbf{u}^h\|_{E(\Omega)}$ is defined as:

$$\|\mathbf{u} - \mathbf{u}^h\|_{E(\Omega)} = \left(\frac{1}{2}\int_{\Omega} (\boldsymbol{\varepsilon} - \boldsymbol{\varepsilon}^h)^T \mathbf{C}(\boldsymbol{\varepsilon} - \boldsymbol{\varepsilon}^h)\, d\Omega\right)^{1/2}. \tag{4.24}$$

In Table 4.3, it is seen that the relative error norms in displacement and in energy are 10^{-4} and 10^{-3}, respectively. These are comparable to the patch test results obtained in Section 4.4.2, and again, the disagreement with the exact solution is due to numerical integration errors.

4.4.3 Infinite Plate with a Circular Hole

An infinite plate with a traction free circular hole under unidirectional tension along x_1 is considered (Fig. 4.6). The exact solution to this problem is given in Timoshenko and Goodier (1970) as well as Szabó and Babuška (1991). The domain $ABCDE$ shown in Fig. 4.6 is modeled with the exact tractions imposed along BC and CD.

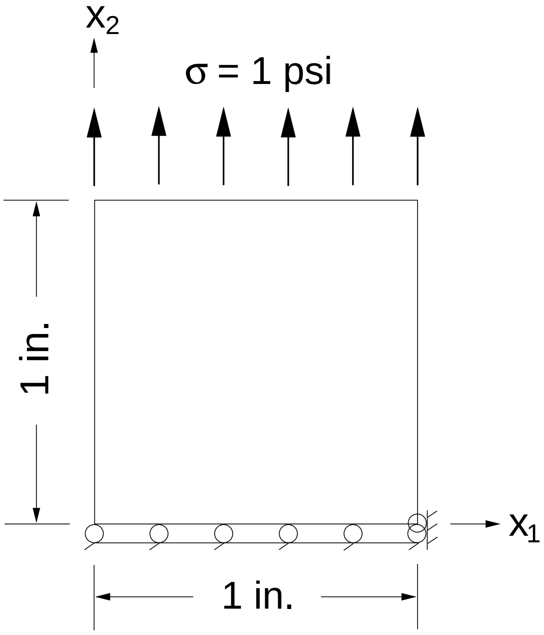

Figure 4.5: Equilibrium (uniaxial tension) patch test.

Table 4.3: Relative error norms for the equilibrium patch test.

Grids	Quadrature	$\dfrac{\lVert\mathbf{u}-\mathbf{u}^h\rVert_{L^2(\Omega)}}{\lVert\mathbf{u}\rVert_{L^2(\Omega)}}$	$\dfrac{\lVert\mathbf{u}-\mathbf{u}^h\rVert_{E(\Omega)}}{\lVert\mathbf{u}\rVert_{E(\Omega)}}$
a	3	1.8×10^{-3}	4.5×10^{-3}
	25	1.7×10^{-4}	4.4×10^{-4}
c	3	8.2×10^{-3}	3.2×10^{-2}
	25	1.4×10^{-3}	4.0×10^{-3}
e	3	6.1×10^{-3}	9.5×10^{-2}
	25	8.8×10^{-4}	6.9×10^{-3}

Due to symmetry, the essential boundary conditions are: $u_2 = 0$ along AB, and $u_1 = 0$ along DE. In polar coordinates (r, θ), the exact stress distribution for $\sigma_0 = 1$ psi is

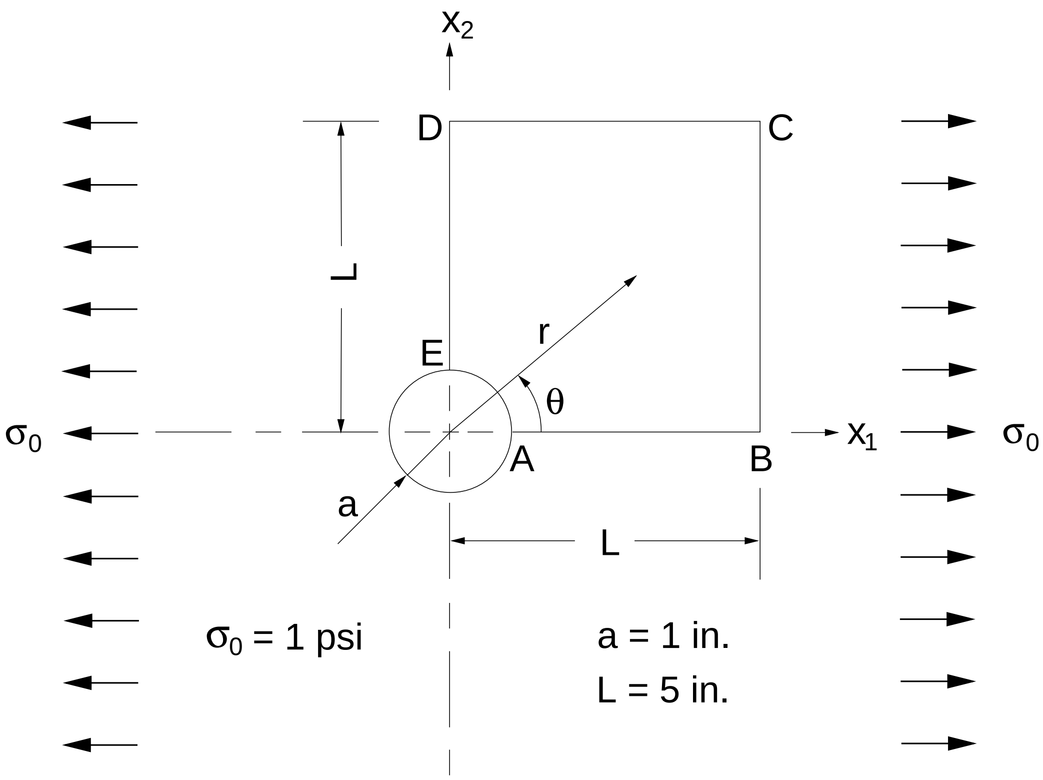

Figure 4.6: Plate with a circular hole under tension.

given by

$$\sigma_{11}(r,\theta) = 1 - \frac{a^2}{r^2}\left(\frac{3}{2}\cos 2\theta + \cos 4\theta\right) + \frac{3}{2}\frac{a^4}{r^4}\cos 4\theta, \tag{4.25a}$$

$$\sigma_{22}(r,\theta) = -\frac{a^2}{r^2}\left(\frac{1}{2}\cos 2\theta - \cos 4\theta\right) - \frac{3}{2}\frac{a^4}{r^4}\cos 4\theta, \tag{4.25b}$$

$$\sigma_{12}(r,\theta) = -\frac{a^2}{r^2}\left(\frac{1}{2}\sin 2\theta + \sin 4\theta\right) + \frac{3}{2}\frac{a^4}{r^4}\sin 4\theta, \tag{4.25c}$$

where a is the radius of the circular hole. The displacement components (rigid-body displacement and rotation set to zero) are:

$$u_1(r,\theta) = \frac{a}{8\mu}\left[\frac{r}{a}(\kappa+1)\cos\theta + 2\frac{a}{r}((1+\kappa)\cos\theta + \cos 3\theta) - 2\frac{a^3}{r^3}\cos 3\theta\right], \quad (4.26a)$$

$$u_2(r,\theta) = \frac{a}{8\mu}\left[\frac{r}{a}(\kappa-3)\sin\theta + 2\frac{a}{r}((1-\kappa)\sin\theta + \sin 3\theta) - 2\frac{a^3}{r^3}\sin 3\theta\right], \quad (4.26b)$$

where μ is the shear modulus and κ (Kolosov constant) is defined as

$$\kappa = \begin{cases} 3-4\nu & \text{(plane strain)}, \\ \dfrac{3-\nu}{1+\nu} & \text{(plane stress)}. \end{cases} \quad (4.27)$$

In the numerical computations, $a = 1$ in., $L = 5$ in., and plane strain conditions are assumed. The nodal discretizations used in the computations are shown in Fig. 4.7. In Fig. 4.9, the rates of convergence (R) in displacement and energy for NEM and constant strain finite elements are presented. The theoretical convergence rates for the displacements and strains using finite elements (non-singular problems) are $R = 2$ and $R = 1$, respectively (see Eq. (2.33)). It is observed from Fig. 4.9 that the rates of convergence of NEM and FE are about the same, with NEM showing better absolute accuracy in displacements and strains. In Fig. 4.9a, the stress concentration factor ($\sigma_{11}^{exact}/\sigma_0 = 3$) at point E is indicated within parentheses. It is seen that NEM is able to accurately capture the stress concentration at point E. In Fig. 4.8, the numerical and exact normal stress σ_{11} are plotted along the edge ED (see Fig. 4.6). The grid shown in Fig. 4.7c is used, and 240 equi-spaced output points between $r = 1$ in. and $r = 5$ in. are chosen in the computations. Agreement between the NEM and the

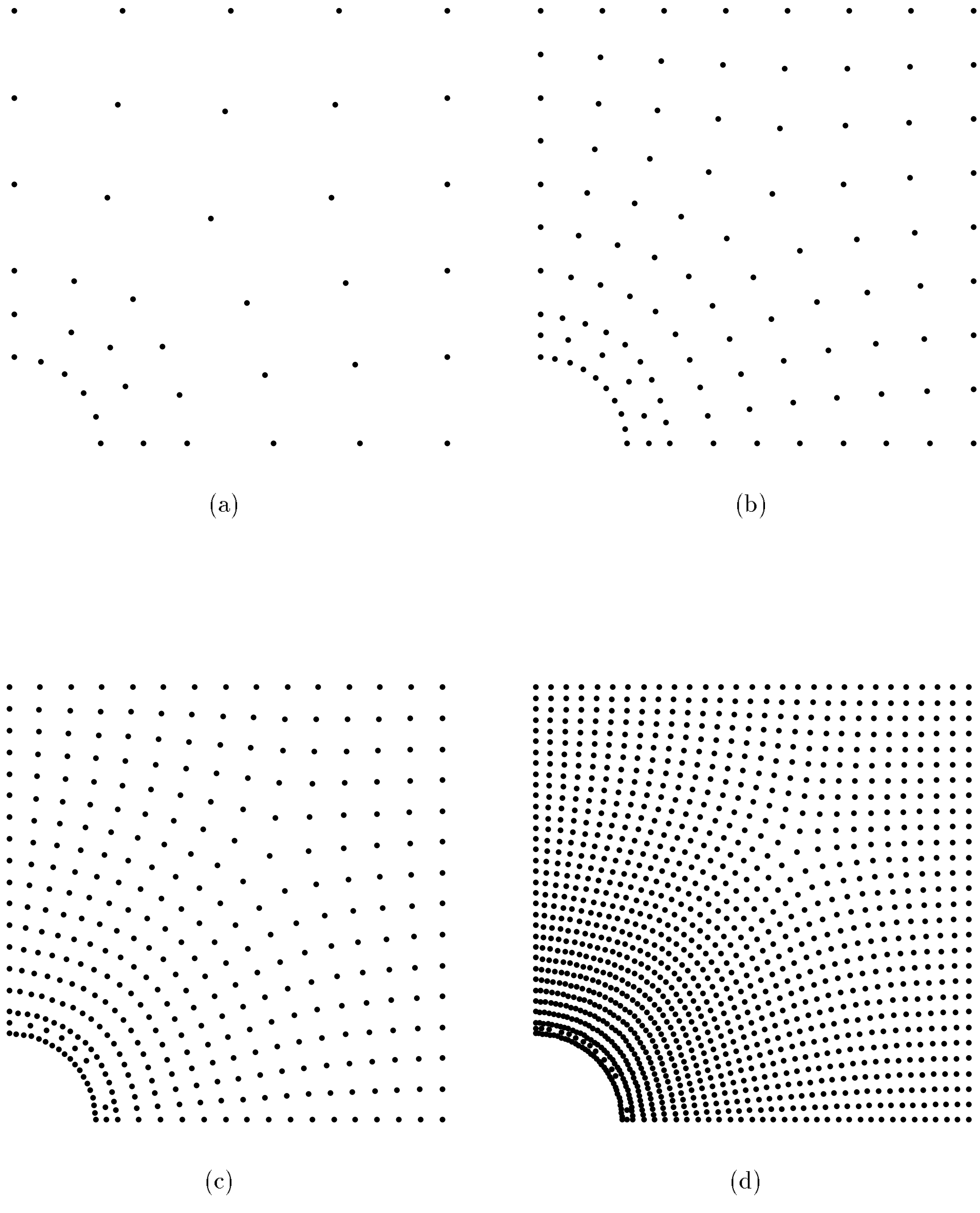

Figure 4.7: Nodal discretization for the plate with a hole problem. (a) 41 nodes, (b) 108 nodes, (c) 361 nodes, and (d) 1345 nodes.

exact stress solution is excellent. The displacement along the edge is linear between two adjacent nodes, and hence one observes the jumps in the stress σ_{11} at the nodes.

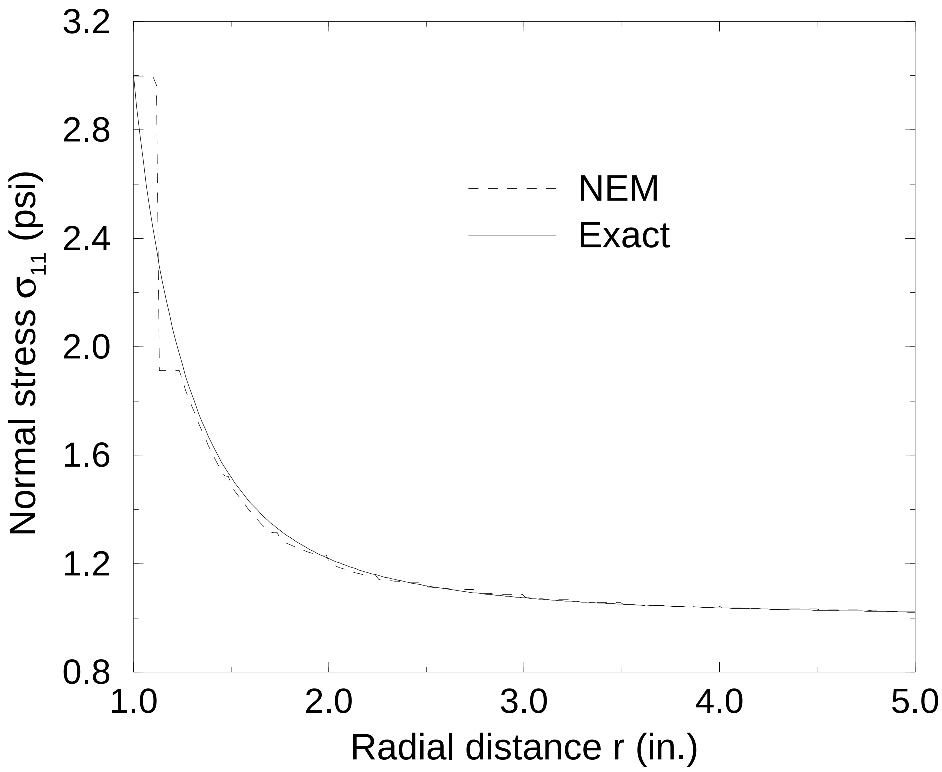

Figure 4.8: Comparison of σ_{11} for NEM and the exact solution along a radial line ($\theta = 90°$).

4.4.4 Cantilever Beam

In Fig. 4.10, a cantilever beam subjected to a parabolic end load is illustrated. The beam has length L, height D, and unit thickness. The displacement vector solution

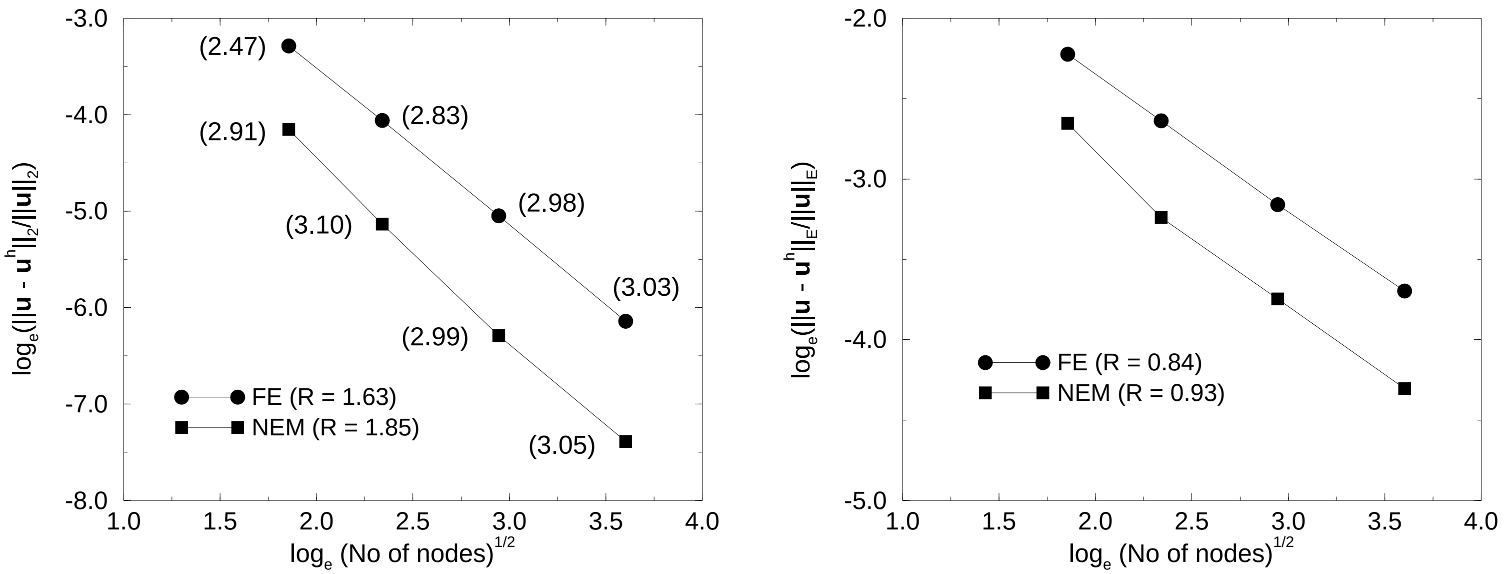

(a) (b)

Figure 4.9: Rate of convergence for the plate with a hole problem. (a) Displacement, and (b) Energy.

is given by (Timoshenko and Goodier, 1970)

$$u_1(x_1,x_2) = \frac{-Px_2}{6\bar{E}I}\left[(6L-3x_1)x_1 + (2+\bar{\nu})x_2^2 - \frac{3D^2}{2}(1+\bar{\nu})\right], \tag{4.28a}$$

$$u_2(x_1,x_2) = \frac{P}{6\bar{E}I}\left[3\bar{\nu}x_2^2(L-x_1) + (3L-x_1)x_1^2\right], \tag{4.28b}$$

where

$$\bar{E} = \begin{cases} E & \text{(plane stress)}, \\ \dfrac{E}{1-\nu^2} & \text{(plane strain)}, \end{cases} \tag{4.29a}$$

$$\bar{\nu} = \begin{cases} \nu & \text{(plane stress)}, \\ \dfrac{\nu}{1-\nu} & \text{(plane strain)}. \end{cases} \tag{4.29b}$$

The stresses are given by

$$\sigma_{11}(x_1,x_2) = \frac{-P(L-x_1)x_2}{I}, \tag{4.30a}$$

$$\sigma_{22}(x_1,x_2) = 0, \tag{4.30b}$$

$$\sigma_{12}(x_1,x_2) = \frac{P}{2I}\left(\frac{D^2}{4} - x_2^2\right), \tag{4.30c}$$

where I is the moment of inertia, which for a beam with rectangular cross-section and unit thickness is:

$$I = \frac{D^3}{12}. \tag{4.30d}$$

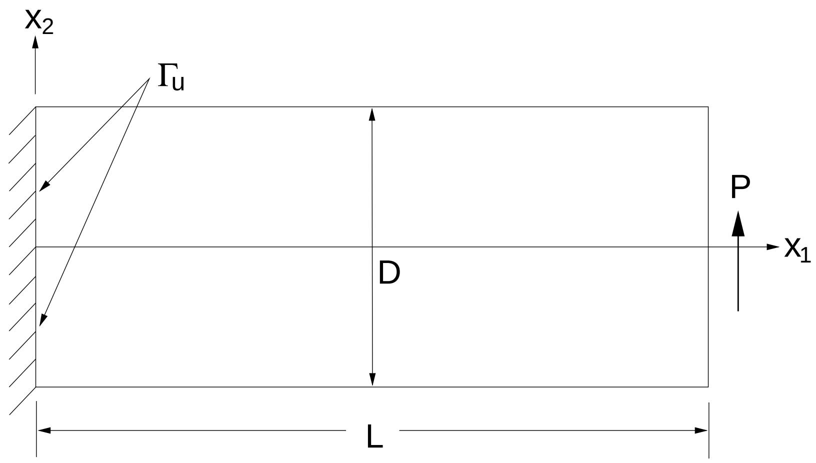

Figure 4.10: Cantilever beam model.

In the numerical model, the analytical displacement solution from Eq. (4.28) is prescribed on the boundary Γ_u: $x_1 = 0$, $-D/2 \leq x_2 \leq D/2$ (Fig. 4.10). On the remaining boundaries, exact tractions are specified. The following parameters are used in the numerical computations: $P = -1000$ lb, $D = 1$ in., $L = 4$ in., and plane stress conditions are assumed.

Convergence studies are carried out using four different nodal discretizations, namely 85 nodes, 297 nodes, 1105 nodes, and 1701 nodes. Equal nodal spacing in the x_1- and x_2-direction is used in each of the above grids. In Fig. 4.11, a sample nodal discretization (85 nodes) is shown. The $L^2(\Omega)$ and energy error norms are calculated on the basis of Eqs. (4.22a) and (4.24), respectively. In Fig. 4.12, the relative displacement and energy error norms are plotted against the nodal spacing h on a log-log plot. The rate of convergence is indicated by the value of R. The convergence rate for NEM is close to the theoretical rate for finite elements, namely $R = 2$ and $R = 1$ for displacements and strains, respectively. The absolute accuracy of NEM is observed to be better than that of the finite element solution.

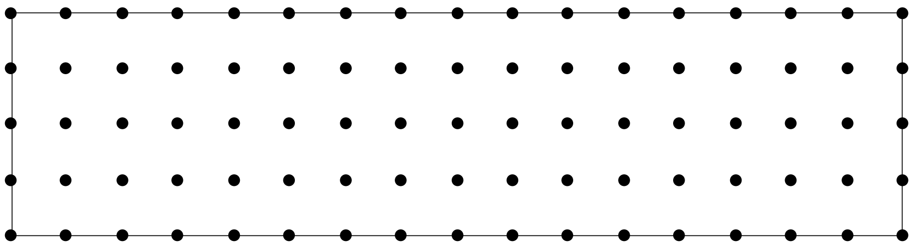

Figure 4.11: Nodal discretization for cantilever beam model (85 nodes).

The NEM and analytical stress fields are compared near the mid-line ($x = 2.03$ in.) of the beam. Since the shape function algorithm chosen here fails for points along $x = 2$ in. (Delaunay edges), such a choice is necessitated. In Fig. 4.13, the normal and shear stresses at $x = 2.03$ in. are plotted as a function of y. The nodal grid consisting of 1105 nodes is used, and the stress outputs are carried out at 200 equi-distant points between $y = -0.5$ in. and $y = 0.5$ in. The NEM and the analytical solution are in good agreement. The maximum error in the normal stress σ_{11} is less than 1%, and the shear stress profile also matches the analytical solution well.

4.4.5 Hollow Cylinder under Internal Pressure

Consider a hollow cylinder of internal and external radius of a and b, respectively. A A uniform pressure p_i is applied to the inner surface ($r = a$), while the outer surface ($r = b$) is traction-free. A schematic of the model problem is shown in Fig. 4.14. Due to axi-symmetry, the stresses are independent of θ, and hence only have a radial dependence. The exact solution for the stress components in polar coordinates (r, θ)

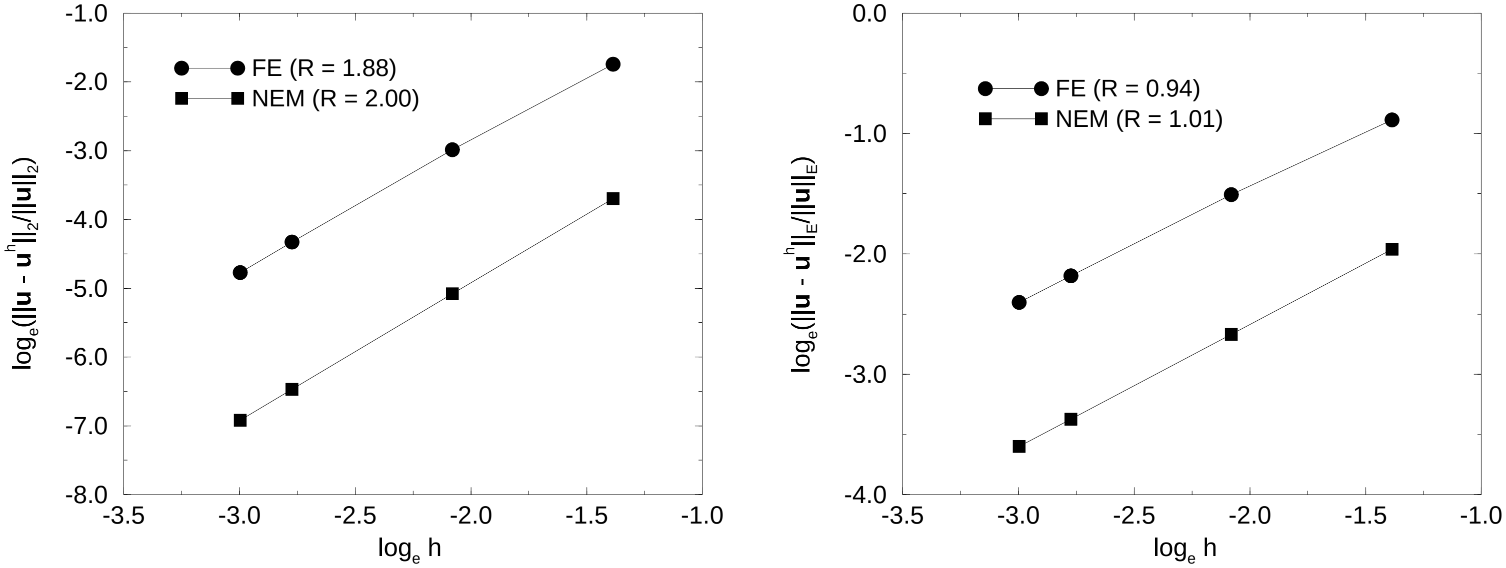

(a) (b)

Figure 4.12: Rate of convergence for the cantilever beam problem. (a) Displacement, and (b) Energy.

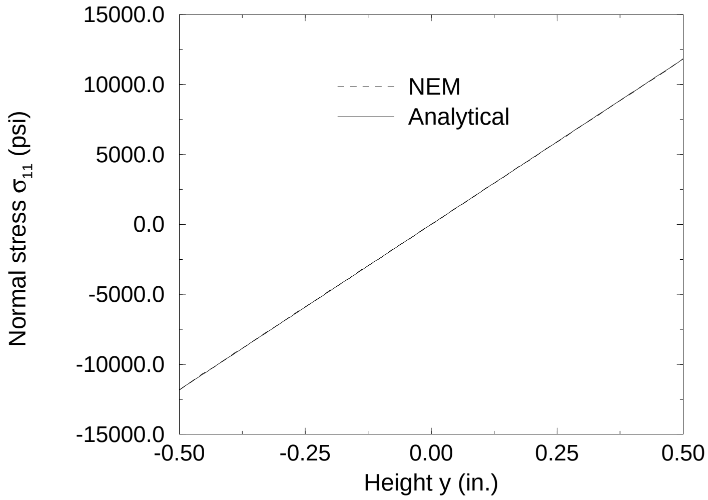

(a)

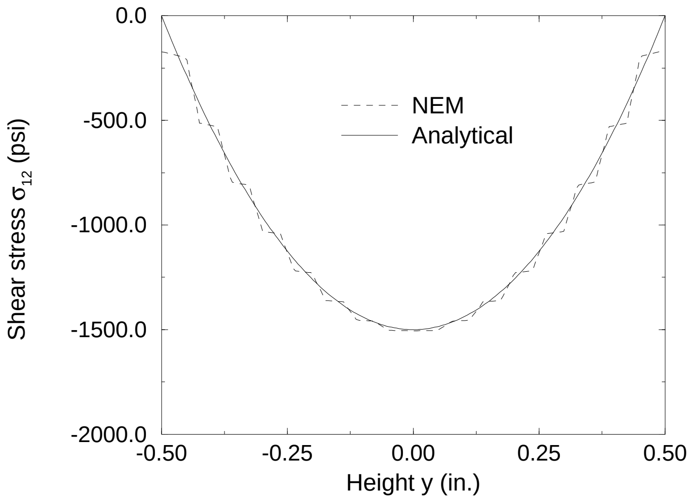

(b)

Figure 4.13: Comparison of NEM and analytical stresses for the cantilever beam model. (a) Normal stress σ_{11}, and (b) Shear stress σ_{12}.

is (Timoshenko and Goodier, 1970):

$$\sigma_r(r) = \frac{a^2 p_i}{b^2 - a^2}\left(1 - \frac{b^2}{r^2}\right), \tag{4.31a}$$

$$\sigma_\theta(r) = \frac{a^2 p_i}{b^2 - a^2}\left(1 + \frac{b^2}{r^2}\right), \tag{4.31b}$$

$$\sigma_{r\theta} = 0. \tag{4.31c}$$

Under plane stress conditions, the components of the small strain tensor are

$$\varepsilon_r(r) = \frac{a^2 p_i}{E(b^2 - a^2)}\left\{1 - \nu - \frac{b^2}{r^2}(1+\nu)\right\}, \tag{4.32a}$$

$$\varepsilon_\theta(r) = \frac{a^2 p_i}{E(b^2 - a^2)}\left\{1 - \nu + \frac{b^2}{r^2}(1+\nu)\right\}, \tag{4.32b}$$

$$\varepsilon_{r\theta} = 0, \tag{4.32c}$$

while the radial and tangential displacements are given by

$$u_r(r) = \frac{a^2 p_i r}{E(b^2 - a^2)}\left\{1 - \nu + \frac{b^2}{r^2}(1+\nu)\right\}, \tag{4.33a}$$

$$u_\theta = 0. \tag{4.33b}$$

In the numerical computations, the following parameters are chosen: $a = 1$ in., $b = 5$ in., $p_i = 3 \times 10^4$ psi, and plane stress conditions are assumed. Due to symmetry, only one-quarter of the specimen is modeled. In the analyses, six different nodal discretizations are considered, namely, 169 nodes, 361 nodes, 625 nodes, 1369 nodes, 1849 nodes, and 2401 nodes. In Fig. 4.15, the nodal grids for 169 and 625 nodes are illustrated. A convergence study is carried out using the above six nodal

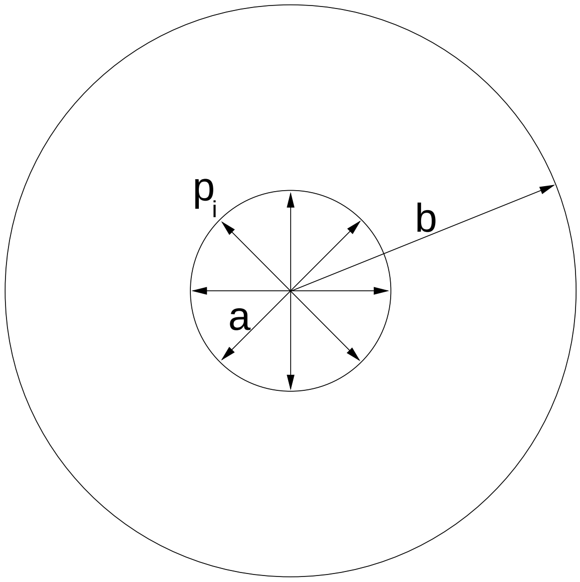

Figure 4.14: Hollow cylinder under internal pressure p_i.

discretizations. The exact $L^2(\Omega)$ and energy norms are given by

$$\|\mathbf{u}\|_{L^2(\Omega)} = \alpha\sqrt{\frac{\pi}{2}}\sqrt{\frac{(1-\nu)^2(b^4-a^4)}{4} + (1-\nu^2)b^2(b^2-a^2) + b^4(1+\nu)^2 \log\frac{b}{a}}, \quad (4.34a)$$

$$\|\mathbf{u}\|_{E(\Omega)} = \alpha\sqrt{\frac{\pi E}{4}}\sqrt{(1-\nu)(b^2-a^2) + b^4(1+\nu)\left(\frac{1}{a^2}-\frac{1}{b^2}\right)}, \quad (4.34b)$$

where

$$\alpha = \frac{a^2 p_i}{E(b^2-a^2)}. \quad (4.34c)$$

For the specimen dimensions, internal pressure p_i, and material properties that are considered here, $\|\mathbf{u}\|_{L^2(\Omega)} = 2.462 \times 10^{-3}$ in^2 and $\|\mathbf{u}\|_{E(\Omega)} = 5.605 \sqrt{\text{psi-in}^2}$. In Fig. 4.16, the convergence rate (R) in displacement and energy are presented for NEM and constant strain finite elements. The trends are similar to that observed in

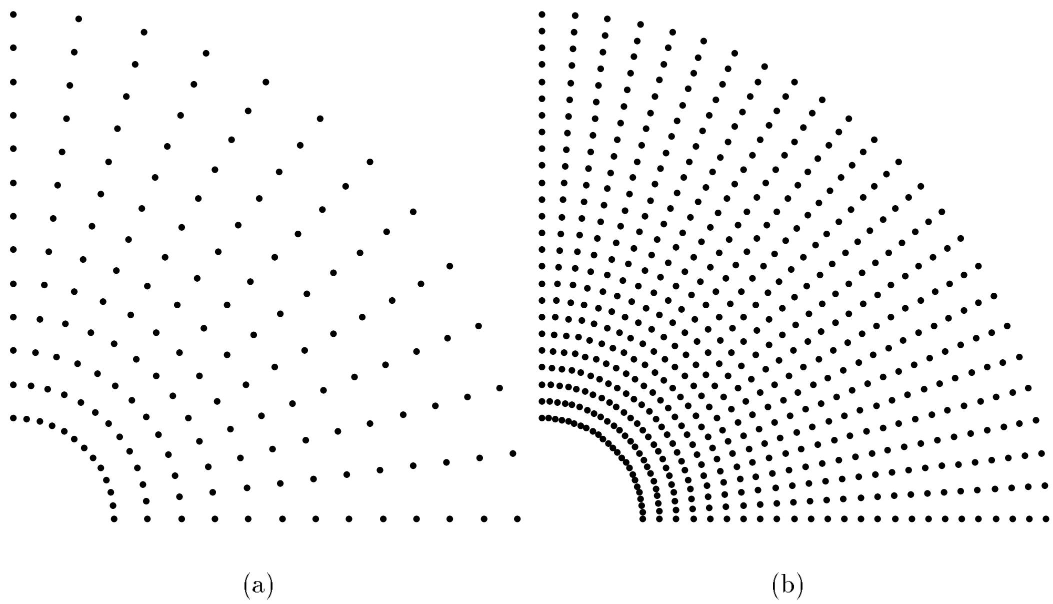

Figure 4.15: Sample nodal discretizations for the hollow cylinder under internal pressure problem. (a) 169 nodes, and (b) 625 nodes.

the earlier examples, with similar rates for NEM and FE, with NEM showing better absolute accuracy in displacements and strains.

A comparison of the NEM and exact stress fields is carried out using the grid consisting of 1369 nodes. The numerical solution recovered the rotational symmetry of the solution, and hence for the purpose of comparison, we plot the stresses along a radial line ($\theta = 30°$). In Fig. 4.17, the NEM and exact solutions for the radial stress and the hoop stress are presented. In the computations, 180 equi-distant output points between $r = 1$ in. and $r = 5$ in. are considered. The NEM and exact stress fields are in good agreement. Since the NEM displacement field is C^0 at the nodes, the numerical stresses are oscillatory. However, the oscillations are bounded, and they fluctuate about the exact solution, which is analogous to the finite element method,

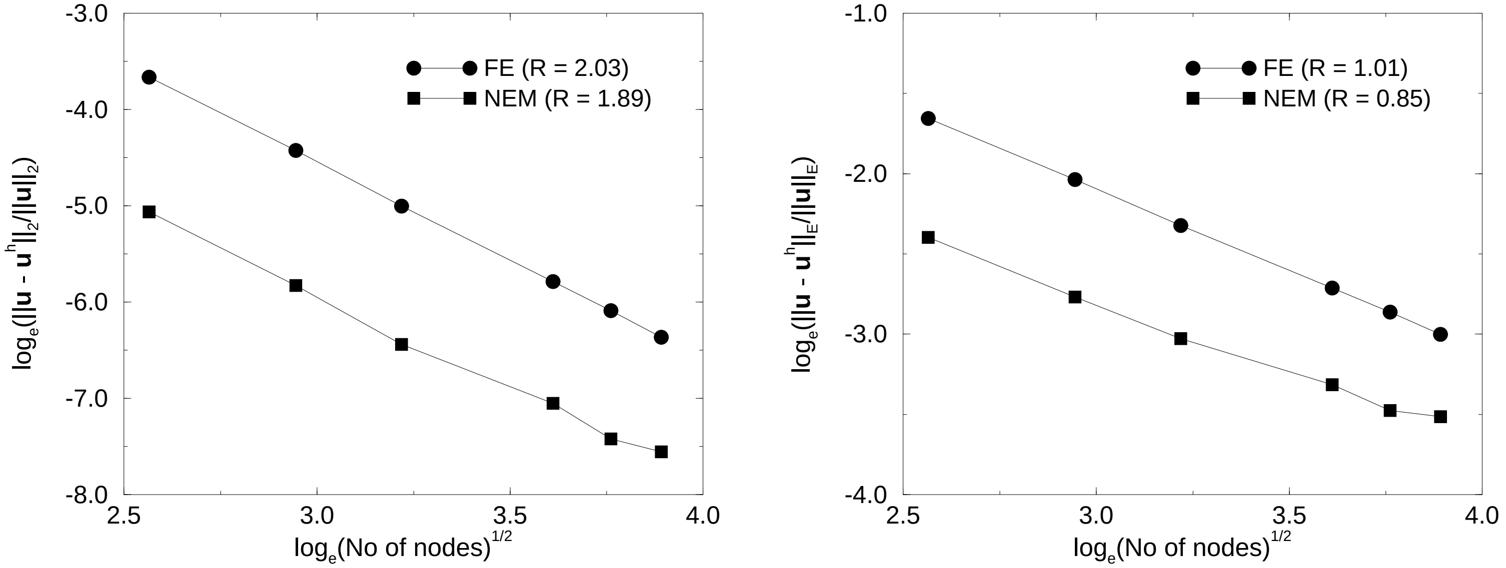

(a)

(b)

Figure 4.16: Rate of convergence for the hollow cylinder under internal pressure problem. (a) Displacement, and (b) Energy.

where the stresses are discontinuous across element boundaries.

4.4.6 Infinite Plate with an Inclusion

We consider the problem of an inclusion (α-phase) with a constant eigenstrain $\boldsymbol{\varepsilon}^*_\alpha$ in an infinite matrix (β-phase). In Fig. 4.18, a graphical representation of the problem is illustrated. The exact displacement vector solution in polar coordinates is given by (Mura, 1987)

$$u_r(r) = \begin{cases} C_1 r & r \leq R, \\ C_1 \dfrac{R^2}{r} & r \geq R, \end{cases} \tag{4.35a}$$

$$u_\theta = 0, \tag{4.35b}$$

where

$$C_1 = \frac{(\mu^\alpha + \lambda^\alpha)\bar{\varepsilon}^*_\alpha}{\mu^\alpha + \lambda^\alpha + \mu^\beta}. \tag{4.36}$$

In the above equation, μ and λ are the Lamé constants of the respective phases, while the eigenstrain $\bar{\varepsilon}^*_\alpha$ is a constant dilatational strain. The material properties used in the numerical computation are (Cordes and Moran, 1996): $\lambda^\alpha = 497.16$, $\mu^\alpha = 390.63$ in the α-phase, while the constants in the β-phase are $\lambda^\beta = 656.79$, $\mu^\beta = 338.35$. These correspond to $E^\alpha = 1000$, $\nu^\alpha = 0.28$, $E^\beta = 900$, and $\nu^\beta = 0.33$. A constant dilatational eigenstrain $\bar{\varepsilon}^*_\alpha = 0.01$ is assumed in the analysis, and the associated eigenstrain tensor is $\boldsymbol{\varepsilon}^*_\alpha = \bar{\varepsilon}^*_\alpha(\mathbf{e}_1\mathbf{e}_1 + \mathbf{e}_2\mathbf{e}_2)$.

The numerical model (quarter symmetry) is shown in Fig. 4.19, where the nodal

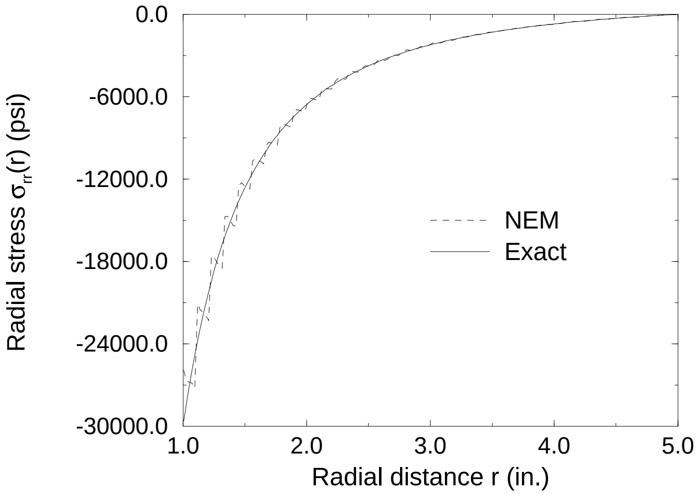

(a)

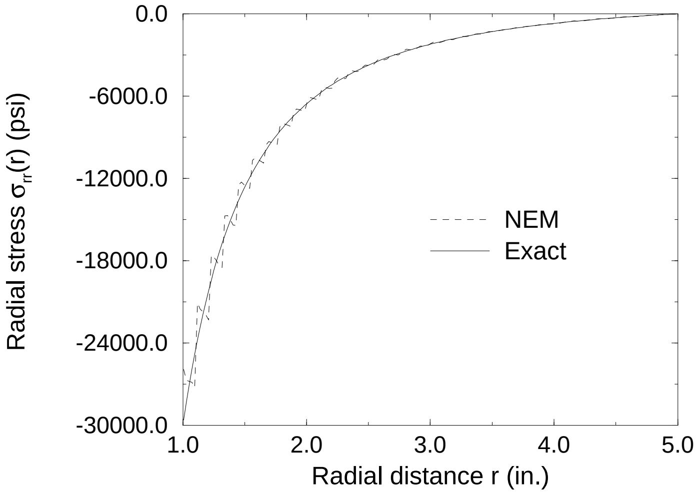

(b)

Figure 4.17: Comparison of the radial and hoop stresses for the hollow cylinder under internal pressure problem. (a) Radial stress $\sigma_{rr}(r)$, and (b) Hoop stress $\sigma_{\theta\theta}(r)$.

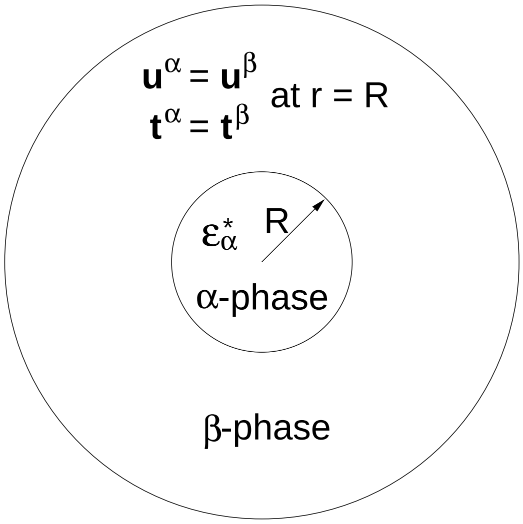

Figure 4.18: Inclusion embedded in an infinite matrix.

discretization consists of 647 nodes, with 114 nodes in the inclusion, 520 nodes in the matrix, and 13 nodes along the interface $r = R$. The outer radius $R_0 = 200$ is sufficiently large in comparison to the radius of the inclusion $R = 5$, so as to adequately represent the infinite matrix. Essential boundary conditions are imposed along the lines of symmetry, while the outer radius $R_0 = 200$ is traction-free. Plane strain conditions are assumed in the numerical computations. The NEM solution recovered the cylindrical symmetry in the solution, and hence results are presented as a function of only the radial distance. The maximum error in the numerically computed tangential displacement u_θ and shear stress $\sigma_{r\theta}$ are $\mathcal{O}(10^{-5})$ and $\mathcal{O}(10^{-4})$, respectively. In Fig. 4.20, a comparison of the NEM and exact solution is presented. The results shown in Fig. 4.20 are computed along a radial line ($r = 0$ to $r = 100$) at $\theta = 30°$. Along the radial line, 30 equi-spaced output points are chosen within the inclusion, and 150 equi-spaced points in the matrix. Excellent agreement between the NEM and the analytical solution is observed. The slight discrepancy in $u_r(r)$

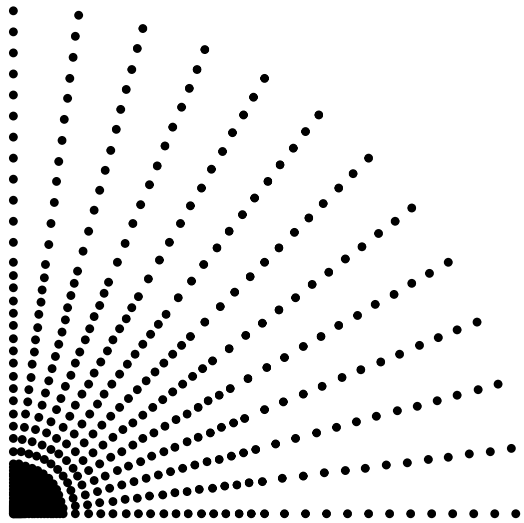

(a)

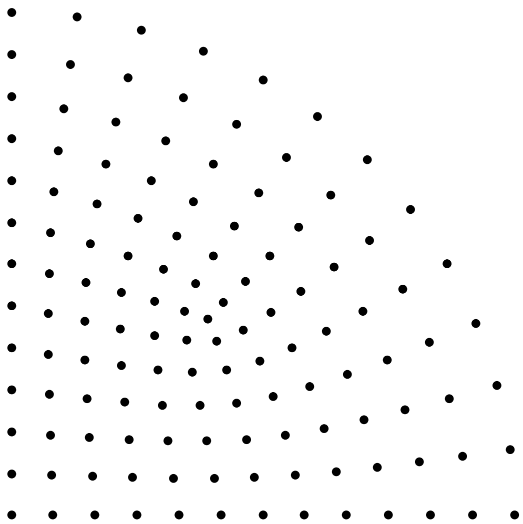

(b)

Figure 4.19: Nodal discretization for inclusion in an infinite matrix problem. (a) Quarter model, (b) Inclusion (α phase).

at $r > 25$ is due to the finite-dimension of the matrix as opposed to the theoretical solution which is based on an infinite matrix. The strains as well as the stresses are in good agreement with the exact solution. The oscillations in the radial and hoop strains are negligible; they are, however, a bit more pronounced in the stress solutions.

4.4.7 Edge-Cracked Plate under Tension

An edge-cracked plate under pure mode I loading is considered. Due to symmetry, only the upper-half is modeled. In Fig. 4.21a, the specimen dimensions and loading are indicated; the crack length a is half of the plate width w. Since the domain is convex, no modifications are required in the implementation of NEM. The mode I stress intensity factors (SIFs) are computed using the domain integral (Moran and Shih, 1987) form of the contour J-integral.

Three different nodal discretizations are considered: a regular grid consisting of 99 nodes shown in Fig. 4.21a and irregular grids of 278 and 2678 nodes with focused array of nodes in the vicinity of the crack-tip (Figs. 4.21b and 4.21c). In Fig. 4.21b, the minimum nodal spacing is $0.006a$, and for the nodal discretization shown in Fig. 4.21c, the minimum nodal spacing is $0.0014a$. In Table 4.4, the normalized mode I stress intensity factors for the three grids are presented. The reference solution for this edge-crack problem is: $K_I^{ref}/\sigma\sqrt{\pi a} = 2.8264$ (Tada, Paris, and Irwin, 1977). From Table 4.4, it is seen that the SIFs computed using NEM are more accurate than the corresponding values evaluated by constant strain finite elements. Domain independence is also clearly observed for the NEM results. The SIFs obtained using NEM for the refined grid (Fig. 4.21c) are within 0.3% of the reference solution results. The

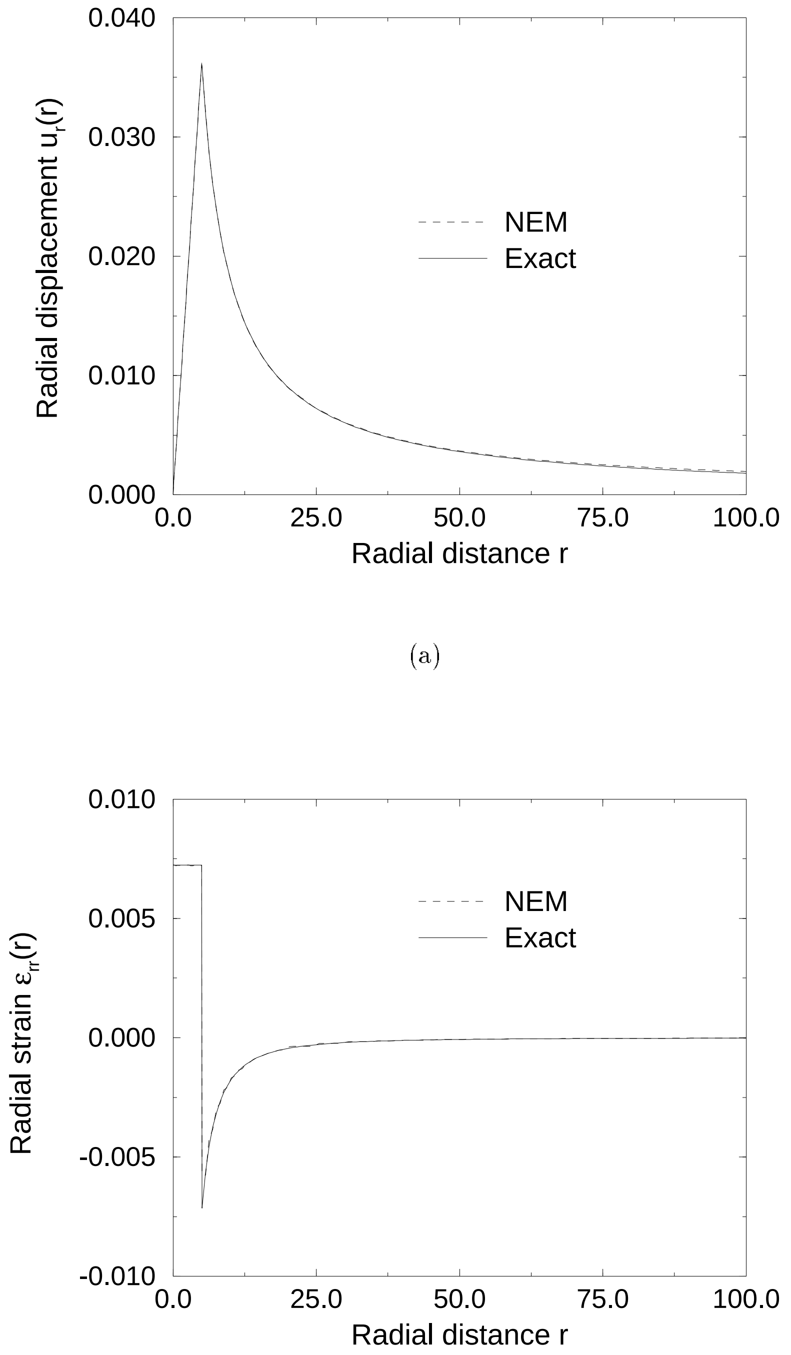
0.040
0.030
0.020
0.010
0.000
Radial displacement $u_r(r)$
NEM
Exact
0.0
25.0
50.0
75.0
100.0
Radial distance r

(a)

0.010
0.005
0.000
-0.005
-0.010
Radial strain $\varepsilon_{rr}(r)$
NEM
Exact
0.0
25.0
50.0
75.0
100.0
Radial distance r

(b)

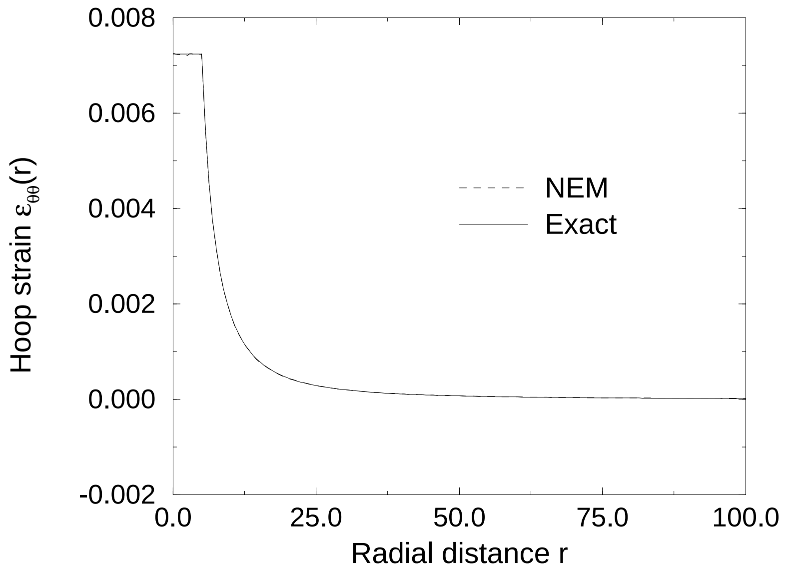

0.008
0.006
0.004
0.002
0.000
-0.002
0.0
25.0
50.0
75.0
100.0
Hoop strain $\varepsilon_{\theta\theta}(r)$
Radial distance r
NEM
Exact

(c)

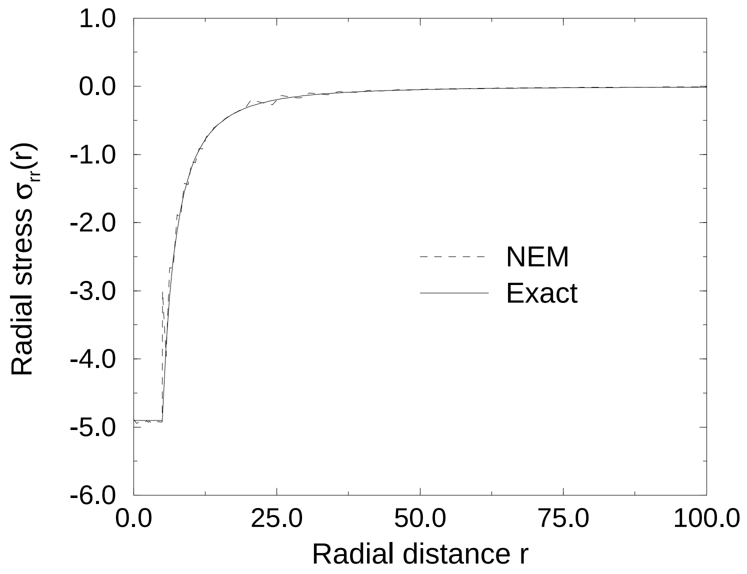

1.0
0.0
-1.0
-2.0
-3.0
-4.0
-5.0
-6.0
0.0
25.0
50.0
75.0
100.0
Radial stress $\sigma_{rr}(r)$
Radial distance r
NEM
Exact

(d)

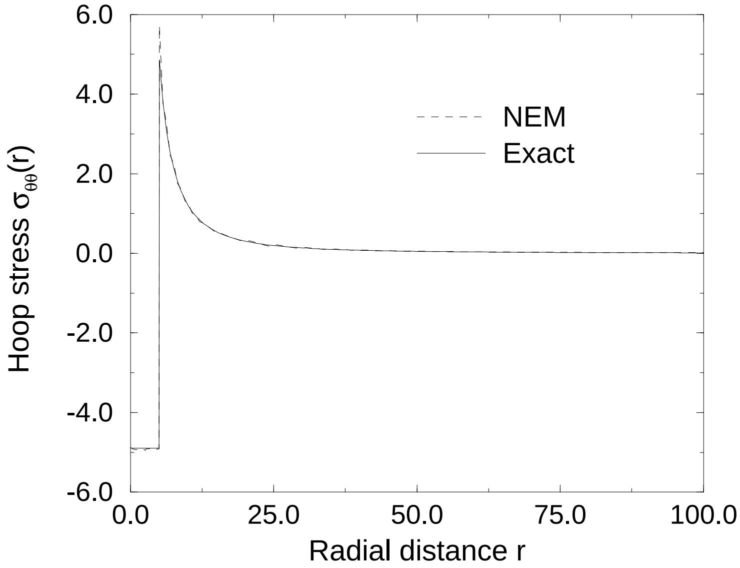

(e)

Figure 4.20: Comparison of NEM and the exact solution for an inclusion with a dilatational eigenstrain in an infinite matrix. (a) Radial displacement $u_r(r)$, (b) Radial strain $\varepsilon_{rr}(r)$, (c) Hoop strain $\varepsilon_{\theta\theta}(r)$, (d) Radial stress $\sigma_{rr}(r)$, and (e) Hoop stress $\sigma_{\theta\theta}(r)$.

domain independence of the SIFs using NEM and the excellent agreement with the reference solution results are encouraging and promising indicators for the application of NEM to SIF evaluation for 2D crack problems.

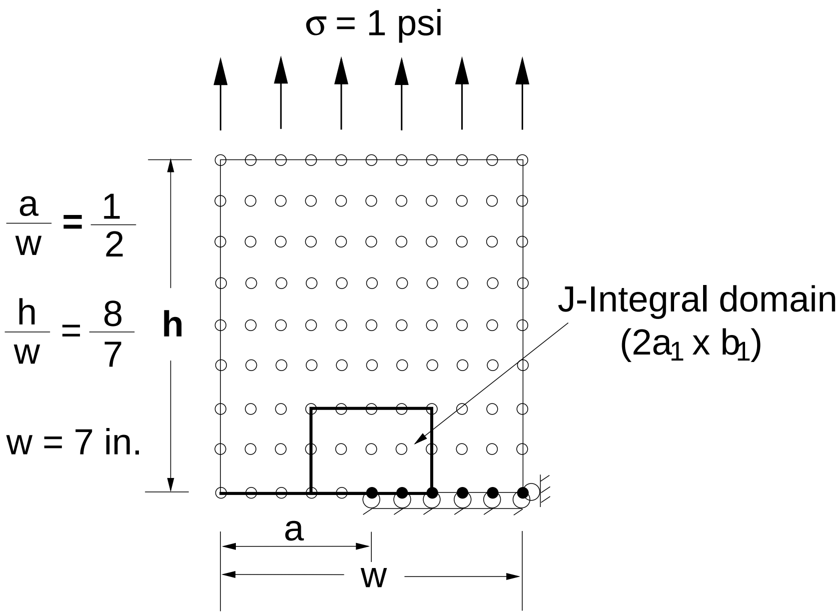

(a)

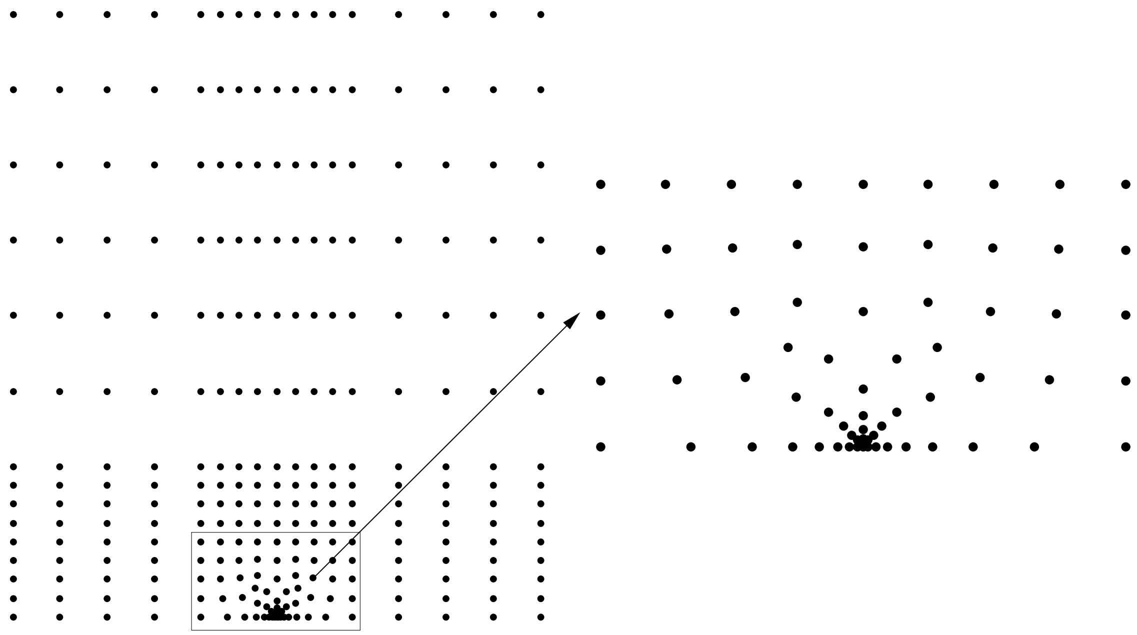

(b)

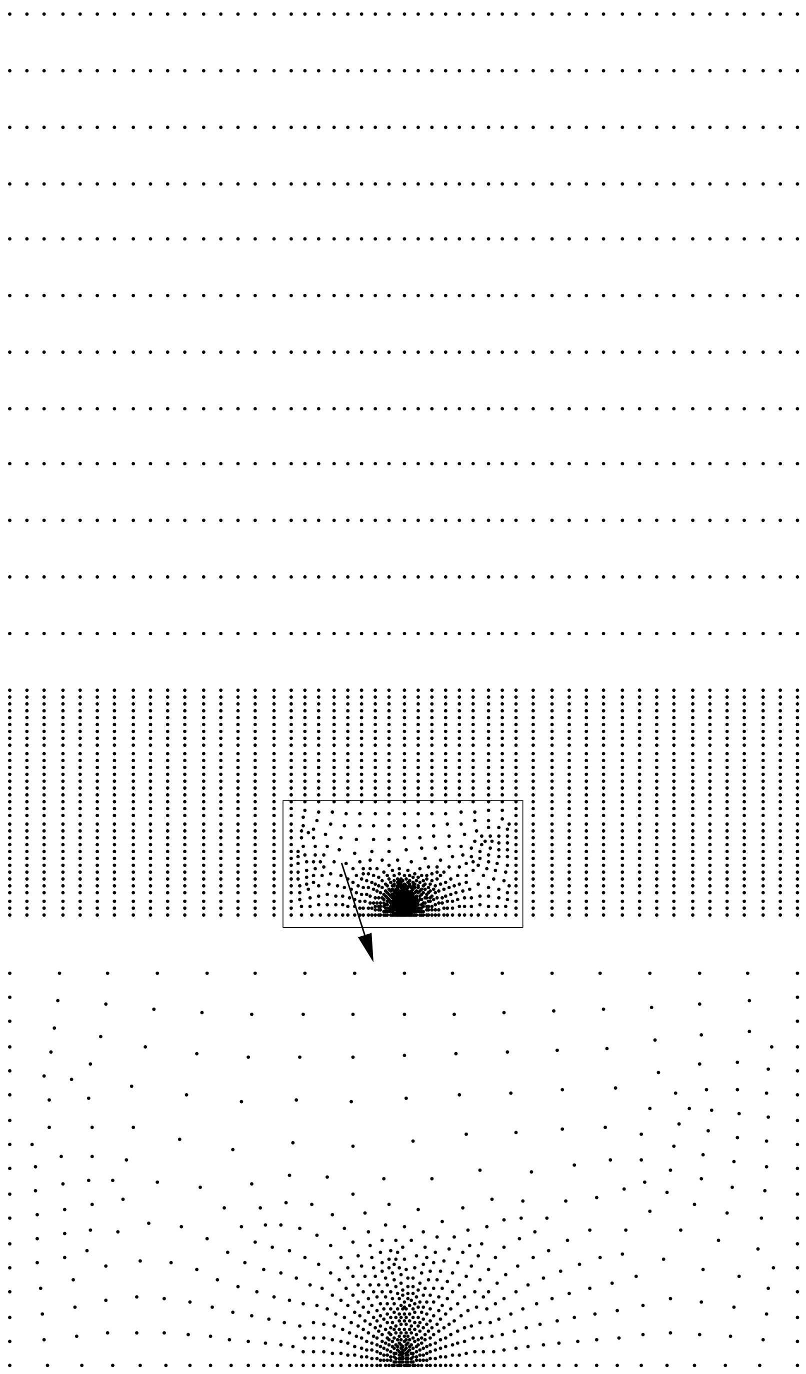

(c)

Figure 4.21: Edge-cracked plate under tension. (a) Regular grid (99 nodes), (b) Refined grid (278 nodes), and (c) Refined grid (2678 nodes)

Table 4.4: Normalized K_I: Edge-cracked plate under tension.

Nodal Grid	Domains a_1	Domains b_1	$\frac{K_I}{\sigma\sqrt{\pi a}}$ [NEM]	% Error	$\frac{K_I}{\sigma\sqrt{\pi a}}$ [FE]	% Error
Regular (99 nodes)	2.8	3.0	2.5241	10.7	2.1159	25.1
	2.8	5.0	2.5360	10.3	2.1691	23.3
	3.5	5.0	2.5310	10.5	2.1664	23.3
	3.5	6.0	2.5339	10.4	2.1806	22.8
	3.5	8.0	2.5375	10.2	2.1989	22.2
Refined (278 nodes)	1.0	2.0	2.7867	1.4	2.6567	6.0
	1.0	4.0	2.7893	1.3	2.6569	6.0
	1.0	6.0	2.7905	1.3	2.6586	5.9
	1.0	8.0	2.7911	1.2	2.6597	5.9
	3.5	8.0	2.7867	1.4	2.6752	5.3
Refined (2678 nodes)	1.0	2.0	2.8188	0.27	2.8052	0.75
	1.0	4.0	2.8188	0.27	2.8047	0.77
	1.0	6.0	2.8189	0.27	2.8049	0.76
	1.0	8.0	2.8188	0.27	2.8051	0.75
	3.5	8.0	2.8188	0.27	2.8051	0.75